The American Journal of Pathology, Vol. 193, No. 11, November 2023

The American Journal of
PATHOLOGY
ajp.amjpathol.org

OCULAR PATHOBIOLOGY

Glial, Neuronal, Vascular, Retinal Pigment Epithelium, and Inflammatory Cell Damage in a New Western Diet—Induced Primate Model of Diabetic Retinopathy

Tailoi Chan-Ling,* Ping Hu,*† Sergio Li Calzi,† Jeff Warner,† Nasir Uddin,*‡ Mariana DuPont,† Martha Neuringer,§ Paul Kievit,¶ Lauren Renner,§ Jonathan Stoddard,‖ Renee Ryals,** Michael E. Boulton,† Trevor McGill,§ and Maria B. Grant†

From the Department of Anatomy, Faculty of Medicine and Health, Bosch Institute, University of Sydney, Camperdown, New South Wales, Australia; the Department of Ophthalmology and Visual Sciences,† University of Alabama, Birmingham, Alabama; the Faculty of Science and Technology,‡ Centre for Research in Therapeutic Solutions, University of Canberra, Bruce, Australian Capital Territory, Australia; and the Departments of Neuroscience§ and Ophthalmology,** the Division of Cardiometabolic Health,¶ and the Integrated Pathology Core,‖ Oregon National Primate Research Center, Oregon Health and Science University, Beaverton, Oregon*

Accepted for publication February 16, 2023.

Address correspondence to Maria B. Grant, M.D., Department of Ophthalmology and Visual Sciences, University of Alabama at Birmingham, 1670 University Blvd., VH490, Birmingham, AL 35233; or Tailoi Chan-Ling, Ph.D., Department of Anatomy, Faculty of Medicine and Health, Bosch Institute, University of Sydney, Camperdown, NSW, Australia.
E-mail: mariagrant@uabmc.edu or tailoi.chan-ling@outlook.com.

This study investigated retinal changes in a Western diet (WD)—induced nonhuman primate model of type 2 diabetes. Rhesus nonhuman primates, aged 15 to 17 years, were fed a high-fat diet ($n = 7$) for >5 years reflective of the traditional WD. Age-matched controls ($n = 6$) were fed a standard laboratory primate diet. Retinal fundus photography, optical coherence tomography, autofluorescence imaging, and fluorescein angiography were performed before euthanasia. To assess diabetic retinopathy (DR), eyes were examined using trypsin digests, lipofuscin autofluorescence, and multimarker immunofluorescence on cross-sections and whole mounts. Retinal imaging showed venous engorgement and tortuosity, aneurysms, macular exudates, dot and blot hemorrhages, and a marked increase in fundus autofluorescence. Post-mortem changes included the following: decreased CD31 blood vessel density ($P < 0.05$); increased acellular capillaries ($P < 0.05$); increased density of ionized calcium-binding adaptor molecule expressing amoeboid microglia/macrophage; loss of regular distribution in stratum and spacing typical of ramified microglia; and increased immunoreactivity of aquaporin 4 and glial fibrillary acidic protein ($P < 0.05$). However, rhodopsin immunoreactivity ($P < 0.05$) in rods and neuronal nuclei antibody—positive neuronal density of 50% ($P < 0.05$) were decreased. This is the first report of a primate model of DR solely induced by a WD that replicates key features of human DR. *(Am J Pathol 2023, 193: 1789—1808; https://doi.org/10.1016/j.ajpath.2023.02.019)*

The worldwide epidemic of type 2 diabetes (T2D) and accompanying diabetic retinopathy (DR) is predicted to increase substantially in the coming years. Western diets (WDs) and sedentary lifestyles often lead to hyperlipidemia, which is associated with macrophage activation and chronic low-grade inflammation.[1–3] This chronic inflammation is further associated with insulin resistance in adipose, muscle, and liver tissue, a hallmark feature of T2D.[4,5] DR, the most common microvascular complication of diabetes, is the major cause of blindness in working age adults worldwide. More than 60% of

Supported by Research to Prevent Blindness (unrestricted departmental funds; M.B.G.); Vision Science Research Center core grant P30 EY003039 (M.B.G.); NIH grants R01EY032753, R01EY025383, R01EY028858, R01EY012601, R01EY028037, EY012601, EY007739, EY025383, EY028858, and HL110170 (M.B.G.); National Health and Medical Research Council Principal Research Fellowship 1005730 (T.C.-L.); Baxter Charitable Foundation grant (T.C.-L.); The Ronald Geoffrey Arnott Foundation grant (T.C.-L.); National Primate Research Center grant P51 OD011092 (M.N.); and Oregon National Primate Research Center Core grant (M.N.).

T.C.-L. and P.H. contributed equally to this work.

Disclosures: None declared.

https://doi.org/10.1016/j.ajpath.2023.02.019

the individuals with 20 years of T2D develop DR.[6] The pathogenesis of DR currently remains incompletely understood and has limited treatment options. Validated animal models that exhibit the full spectrum of retinal pathology are highly valuable to investigate the pathogenesis of DR and foster the development of therapeutics for human DR. Commonly used animal models of DR include diabetic mice and rats; however, these are severely limited in that they do not develop advanced disease, do not have a macula, and have significant differences in the mechanism of retinal vascular formation from humans.[7]

Investigation of primate models of genetic T2D has shown the presence of vascular changes like human DR, including areas of capillary nonperfusion, microaneurysms, cotton-wool spots, intraretinal hemorrhages, and macular hard exudates.[8–11] However, studies in diabetic nonhuman primate (NHP) models have been limited because primates typically require >10 years of diabetes before exhibiting retinal vascular changes and are costly because of the low birth rate.[12] Although both type 1 diabetes models[13] and T2D models have been identified,[9,10] studies have focused primarily on examination of vascular changes.

The current study describes a novel NHP model fed a WD and provides both detailed clinical and histologic characterization, including comprehensive *in vivo* retinal imaging and histologic assessment beyond the vasculature to include changes in microglia/macrophages, astrocytes, Müller cells, retinal pigment epithelium (RPE), and the neurons of the retina. Microglial changes in the neural retina were compared with the ciliary body and the choroid.

Materials and Methods

Animals

Thirteen adult rhesus macaques (6 females and 7 males), aged 15 to 17 years, ranging in weight from 4.7 to 19.2 kg, were assigned to the study. Animals were maintained on either a standard chow diet (Fiber Balanced Diet 5000; Purina Mills, St. Louis, MO) containing 14% of calories from fat, 60% of calories from carbohydrates, and 26% of calories from protein; or a WD high in fat and simple carbohydrates (Lab Diet 5L0P; Purina Mills) containing 36.1% of calories from fat, 45.7% of calories from carbohydrates, and 18.2% of calories from protein. Animals were maintained on the WD for a minimum of 5 years, and all developed T2D in the later years, with all animals being classified as diabetic for a minimum of 2 years, as determined by hemoglobin A1c > 6.0%. Six of seven animals (average hemoglobin A1c before insulin treatment of 11.4%) were maintained on long-acting insulin during the studies (glargine, 10 to 34 units per day), whereas one animal did not require insulin. Blood pressure was recorded before and after a procedure, and all diabetic NHPs were found to have elevated pressures.[14] All animal care and procedures were performed according to the Institutional Animal Care and Use Committee at the Oregon National Primate Research Center at Oregon Health and Science University (Beaverton, OR).

Clinical Observation Methods and Procedure

Retinal color fundus, optical coherence tomography, fluorescein angiography, and autofluorescence imaging were undertaken before euthanasia. Rhesus NHPs were anesthetized by an i.m. injection of Telazol (1:1 mixture of tiletamine hydrochloride and zolazepam hydrochloride; 3.5 to 5.0 mg/kg) and maintained with ketamine (1 to 2 mg/kg) as required; or were sedated with ketamine (10 mg/kg intramuscularly) or Telazol (3 to 5 mg/kg intramuscularly) followed by intubation and anesthesia with inhalant isoflurane (1% to 2%) vaporized in oxygen during retinal imaging. Imaging modalities included color fundus photography (FF450; Zeiss, Oberkochen, Germany), spectral domain optical coherence tomography and fundus autofluorescence (Heidelberg Spectralis, Heidelberg, Germany), and fluorescein angiography.

Tissue Processing and Immunofluorescence Histochemistry

A total of 13 pairs of rhesus NHP eyes were collected, including the T2D primates ($n = 7$) and their age-matched controls ($n = 6$), for histologic examination. The eyes were immersion fixed in 4% paraformaldehyde in 0.1 mol/L phosphate buffer (pH 7.4) overnight at 4°C immediately after euthanasia and then transferred into phosphate-buffered saline.

The neural retina and RPE were prepared as retinal whole mounts, as previously described,[15] or for cryostat cross-sections. Briefly, for whole mounts, the retina with the attached RPE was dissected from the sclera, and five to six radial cuts were made to permit the retinal eyecup to be flattened onto a histologic glass slide, placing extra cuts in the parafoveal region because of the higher curvature of the globe at the NHP fovea. Cellular parameters were analyzed utilizing various combinations of double-marker immunofluorescence in the central, middle, and peripheral retina. Frozen sections were prepared from eight animals (controls, $n = 4$; and T2D, $n = 4$) by embedding a part of the posterior eyecup and generating transverse cryostat sections (12 μm thick), allowing analyses of both the retina and choroid in the central, middle, and peripheral regions. These regions are identified as follows: the line from the optic nerve head to the peripheral edge of the retina is equally divided in three distances. The area close to the optic nerve within the first distance is called central. The area close to the peripheral edge within the third distance is called peripheral. The retinal area between the central and the peripheral area is called the middle area.

The following primary antibodies/markers were used on both retinal whole mounts and frozen sections: CD31 (ab9498; Abcam, Cambridge, MA; used at 1:100) for blood

vessels; glial fibrillary acidic protein antibody (GFAP; GA5; Sigma, St. Louis, MO; used at 1:200) for astrocytes; vimentin-Cy3 antibody (C-9080; Sigma-Aldrich, St. Louis, MO; used at 1:100) for Müller cells; aquaporin-4 (AQP4; sc-20812; Santa Cruz Biotechnology, Dallas, TX; used at 1:100) for water channel protein; ionized calcium-binding adaptor molecule-1 (Iba-1; number 19-19741; Wako, Pure Chemical Industries, Osaka, Japan; used at 1:100) for microglia/macrophages; biotinylated *Griffonia simplicifolia* (*Bandeiraea*) isolectin B4 (GS lectin; Sigma-Aldrich; used at 1:200) for blood vessels, microglia, and macrophages; mouse anti-rhodopsin (Rho; MAB 5356; Chemicon, Temecula, CA; used at 1:1000) for photoreceptors; and mouse anti-human neuronal nuclei antibody (NeuN; MAB 377; Chemicon; used at 1:200) for neuronal cell counts. Omission of primary antibody was undertaken as a control experiment for all markers utilized.

Microscopy

For multiple-marker immunofluorescence, retinal whole mounts and frozen sections were examined and imaged using laser-scanning confocal microscopes. Imaging was performed using either a Zeiss LSM 610 or a Zeiss LSM 800 (equipped with Airyscan module) Metaconfocal microscope (Carl Zeiss, Oberkochen, Germany). Images were captured with either the Zeiss LSM 9 610/800 acquisition software or ZEN imaging software version 3.7 (Carl Zeiss) for the two respective microscopes. Z-stack images were collected to provide z projections. The optimal interval, pinhole diameter, and optical depth parameters were consistently maintained as required for the 20× objectives, using an image frame size of 1024 × 1024 pixels. The laser lines were 405, 488, 514, and 633 nm. Scan speed and number of averaged images remained consistent for all images captured in each experiment for both qualitative and quantitative purposes.

For examination of retinal digests, analysis and imaging were undertaken using a Zeiss Axio Imager Upright microscope (Jena, Germany). Images were captured with ZEN imaging software. Image analysis was performed using Adobe Photoshop CS5 software version 12.0 (Adobe Systems, San Jose, CA).

Quantitative Analysis of Relative CD31$^+$ Blood Vessel Density

For relative CD31$^+$ blood vessel density, at least 10 images (20× objective) were taken from each animal eye (two images for the central retina, four images for the mid retina, and four images for peripheral retina) using a Zeiss Axio Imager Upright microscope. The relative CD31$^+$ blood vessel density in the entire image (13.5 × 10 cm) was measured by determining the frequency of positive immunolabeled CD31$^+$ vascular structures coinciding with the intersection of 100 intersection points with a diameter of 0.8 cm in a 13.5 × 10-cm frame superimposed over the image, as reported previously.[16,17]

Trypsin Digest Preparation and Quantitative Analysis of Relative Acellular Capillary Density

Trypsin digests of retinal whole mounts were prepared to permit examination of the frequency of acellular capillary density using the method described by Kuwabara and Cogan,[18] with minor modifications. Retinas were scanned using the Aperio CS slide scanning system with Spectrum Plus information management system (Aperio Technologies Inc., Vista, CA). A total of 10 to 15 random, nonoverlapping fields of retina were imaged (100,000 μm^2). Acellular capillaries >50 μm in length were counted from each image for each retina and expressed relative to control.

Quantitative Analysis of Iba-1$^+$ Microglia/Macrophage Density

For assessment of Iba-1$^+$ microglia/macrophage density, at least five images (10× objective) were taken in each animal (one image for central, two images for mid, and two images for peripheral regions of the retina) for each marker using a Zeiss Axio Imager Upright microscope. The Iba-1$^+$ microglia/macrophage density in the whole area of the image was measured using ImageJ software version 1.53j (NIH, Bethesda, MD, *https://imagej.nih.gov/ij/download.html*). The Iba-1$^+$ microglia/macrophages were determined by both their Iba-1 labeling and their morphology: microglia located primarily in the retina, exhibiting round and irregular somas with a ramified extensive process field; and macrophages located primarily in the ciliary body and choroid, exhibiting larger and irregular somas either without processes or with short processes. For counting purposes, only cell bodies with DAPI counterstaining were analyzed (ie, microglia/macrophage processes without associated cell body were not counted).

Quantitative Analysis of NeuN$^+$ Cell Density

For NeuN$^+$ neuronal cell density, at least three images (40× objective) were taken in each animal using a Zeiss LSM 800 Metaconfocal microscope. The NeuN$^+$ cell density in the whole area of the image was measured using ImageJ software. The NeuN$^+$ cells were determined by their NeuN$^+$ soma labeling and double labeling with DAPI in either the ganglion cell layer or the inner nuclear layer.

Quantitative Analysis of Rho and GFAP/AQP4 Expression

For Rho immunoreactivity, at least three images (20× objective) were taken in each NHP from midperipheral retina. For GFAP and AQP4 immunoreactivity, at least five images (10× objective) were taken from each animal (one image for

central, two images for middle, and two images from peripheral retinal regions) for each marker using a Zeiss Axio Imager Upright microscope. All microscope settings remained consistent for all images captured in each experiment for both qualitative and quantitative purposes. To ensure identical incubation conditions, control and T2D specimens were always stained and imaged together. The immunoreactivity of Rho (intensity) in three to four selected regions was measured, and the intensity of GFAP and AQP4 immunoreactivity in the entire image was measured using ImageJ software.

Quantitative Analysis of Lipofuscin Density in RPE

Lipofuscin is understood to be composed of products resulting from incomplete digestion of photoreceptor outer segments, lipids, and proteins.[19] Lipofuscin also contains fluorophores that autofluoresce when excited by specific wavelengths of light. Lipofuscin autofluorescence can be detected without the need for any labeling with a fluorescent antibody.[20] Transverse frozen sections of control and T2D NHP eyes were prepared as above. These unstained sections were then examined using all four laser lines (405, 488, 514, and 633 nm) to ensure the widest emission spectra of the naturally occurring lipofuscin, to provide a qualitative assessment of lipofuscin density. A minimum of three images (63× objective) were taken in each animal using a Zeiss LSM 800 Metaconfocal microscope. Lipofuscin collections were visible as small round autofluorescent granules with laser light excitation fluorescence emission without prior fluorophore conjugation. The relative density of lipofuscin granules in the RPE in each of the three entire fields of view captured in the central, midperipheral, and peripheral retina was counted by a masked experienced microscopist (P.H.) while utilizing ImageJ software to provide a semiquantitative determination of relative lipofuscin density in control versus high-fat diet fed animals.

Statistical Analysis

To account for variation, the density or immunoreactivity of positive labeling, as determined by brightness of the emission spectra, was normalized by dividing by the mean values of age-matched naïve controls in the same region or tissue and was expressed as the percentage of relative densities for each animal.

Data are reported as means ± SEM. Statistical differences between the high-fat diet fed and age-matched control groups were determined by applying one-tailed *t*-test for unpaired groups with equal variance. $P < 0.05$ was considered statistically significant.

Results

Clinical Observations and Premortem Imaging

Figure 1 shows the premortem imaging of a representative animal maintained on a standard chow diet. Figure 1A is a retinal image from a fluorescein angiogram that shows no breakdown of the blood-retinal barrier and no evidence of retinal pathology. The choroidal flush is evident. Figure 1B shows low-level fundus autofluorescence, which is typically observed in NHPs in this age group. Macular optical coherence tomography (Figure 1, C and D) displays a normal foveal contour and thickness with no evidence of intraretinal or subretinal fluid and no evidence of diabetic macular edema. There is no evidence of foveal atrophic changes or of intraretinal opacities.

The NHPs maintained on a WD demonstrate classic signs of T2D compared with lean animals maintained on standard chow (Figures 2, 3, 4, 5 and 6). Table 1 highlights differences in body weight and body composition for these animals, as well as levels of fasting glucose, homeostatic model assessment for insulin resistance measurements, and hemoglobin A1c when animals are not maintained with exogenous insulin for the treatment of hyperglycemia. The NHPs were maintained on insulin for 2 years before the terminal study. Because of study limitations, the six controls used in this study were not analyzed for body composition or glucose homeostasis. To demonstrate obesity, dyslipidemia, and T2D of the selected obese cohort in this study, reference values of 20 middle-aged male NHPs collected as part of the NHP Obesity Resource at Oregon National Primate Center are provided (Table 1).

In the NHP cohort fed the WD, fundus changes typical of human DR were observed, including venous engorgement and tortuosity (Figure 2), aneurysms (Figure 2 and 3), and macular exudates. The predominant findings, however, were venous tortuosity and leakiness, most marked in the peripheral retina, like that in human DR (Figure 3). Infrequently, there was evidence of changes in the nerve fiber layer suggestive of nerve inflammation and infarcts (Figure 4). By fluorescein angiography, there was evidence of leaky vessels (Figure 5A) and venous tortuosity (Figure 5B). On color fundus images (Figure 6, A–F), there was evidence of venous tortuosity (Figure 6, B, E, and F) and venous beading (Figure 6, C, D, and F). Fundus autofluorescence is shown in Figure 6, G–L, with dot and blot hemorrhages (most prominent in Figure 6, G and I) and venous tortuosity (most prominent in Figure 6, G, H, K, and J). Fluorescein angiography also showed the same vascular pathology (Figure 6, M–R).

$CD31^+$ Blood Vessel Density Decreases while Acellular Capillaries Increase in T2D Retinas

In the retinas of control NHPs, $CD31^+$ blood vessels were distributed in two layers in the central to middle regions of the retina, the superficial (inner) (Figure 7A) and deep (outer) (Figure 7C) retinal plexuses. In the peripheral region, there was only the superficial plexus, similar to the human retinal vasculature.[21] The superficial plexus of $CD31^+$ blood vessels consisted of arteries, veins, and capillaries, whereas the deep intraretinal vascular plexus in the NHPs consisted only of capillary-sized vessels (Figure 7C). In the retinas of

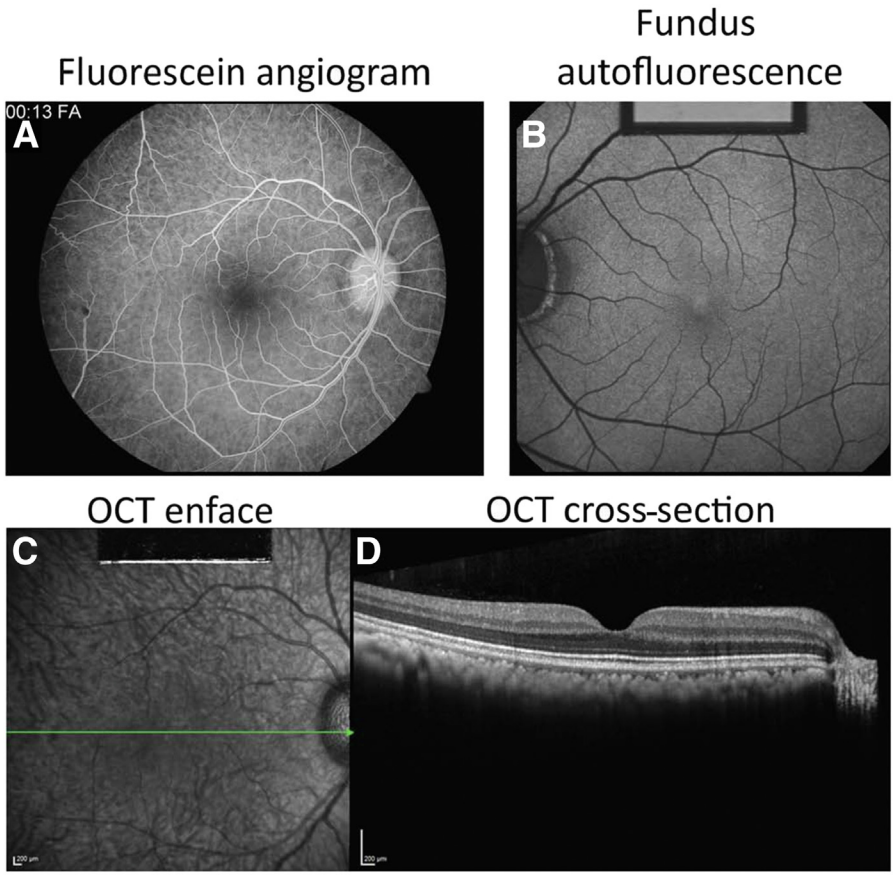

Figure 1 Premortem imaging of a representative control animal maintained on a standard chow diet. **A:** A fluorescein angiogram with no detectable breakdown of the blood-retinal barrier and no evidence of microaneurysms, hemorrhage, or neovascularization. The choroidal flush is evident. **B:** A low level of fundus autofluorescence typically observed in healthy nonhuman primates of this age group. **C:** Macular optical coherence tomography (OCT) displayed a normal foveal contour and thickness with no evidence of intraretinal or subretinal fluid. **C** and **D: Green line** (**C**) represents the level at which the OCT cross-section (**D**) was taken. **D:** There was no evidence of foveal atrophic changes or of intraretinal opacities. Scale bars = 200 μm (**C** and **D**).

the NHPs fed the WD, the density of $CD31^+$ blood vessels of both plexuses decreased (Figure 7, B and D, comparing with Figure 7, A and B), and the capillaries in the outer plexus became noticeably thinner and less bright for CD31 staining compared with control (Figure 7D), suggestive of capillary obliteration or compromised rheology. Blood vessel loss was greatest in the peripheral region of the superficial plexus (inner) and in the central region of deep plexus (outer) (Figure 7, E and F).

Retinal digests, used to count acellular capillaries in control and T2D retinas, indicated a significant increase in the NHP cohort fed the WD (Figure 8, B and D) compared with control NHPs (Figure 8, A and C); quantitative data are shown (Figure 8E). The higher frequency of acellular capillaries in these animals supports the significant vascular regression/occlusion occuring in the WD-fed animals and is consistent with the observed decrease in $CD31^+$ blood vessel density in this group of animals. To characterize the relationship between endothelial cells and microglia/macrophages, vessels were stained with GS lectin and microglia/macrophages were labeled with Iba-1. As shown in Figure 8F, large Iba-1^+ cells interpreted as activated microglia/macrophages were prominent surrounding the blood vessels in the peripheral region of the diabetic retina.

Increased Iba-1^+ Amoeboid Microglia/Macrophage Density, Loss of Regular Stratification, and Spacing of Ramified Microglia in the Retina of WD-Fed Mice

Infrequent Iba-1^+ microglia/macrophage were observed in retinal sections (Figure 9A) and flat mounts (Figure 9C) of control primates. Although Iba-1 labeling does not differentiate between macrophages and ramified microglia (Figure 9C), the morphology of the cell was used to characterize each population. Iba-1^+ ramified cells, characterized as resting microglia, exhibited an extensively ramified process field, showed a regular contact-spacing distribution across the retina, and were located in the retinal ganglion cell layer (Figure 9A) and outer retina with predominantly stratified distribution, as previously reported in humans.[22] Iba-1^+ cells with morphology typical of macrophages were evident between the ganglion cell layer and the inner nuclear layer (Figure 9B).

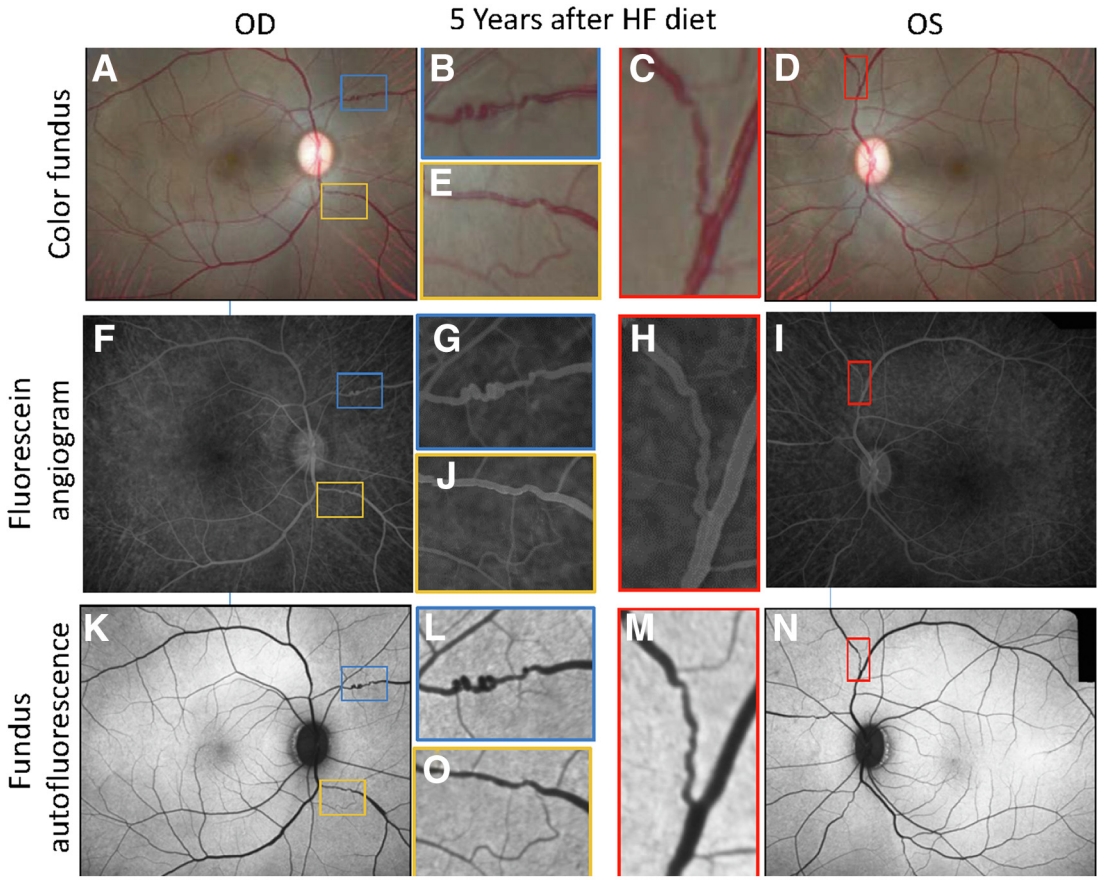

Figure 2 Representative *in vivo* imaging of rhesus macaques fed a high-fat (HF) Western diet (WD) utilizing three image modalities: color fundus, fluorescein angiography, and fundus autofluorescence. Retinal images of a rhesus macaque 5 years following the introduction to WD. **A** and **D:** Color fundus photographs. **B**, **C**, and **E:** Higher-magnification images of the **blue**, **red**, and **yellow boxed areas**, respectively, in **A** and **D**. Attenuation of the blood column with regions of constriction evident at higher magnification in WD-fed nonhuman primates. **F**—**J:** This interpretation is confirmed with fluorescein angiograms with additional evidence of breakdown of the evident due to a loss of clear vessel outlines indicative of leakage of fluorescein into the tissue parenchyma. **G**, **H**, and **J:** Higher magnification images of the **blue**, **red**, and **yellow boxed areas** with marked vessel tortuosity. **K**—**O:** The fundus autofluorescence (**K** and **N**) shows small white exudates in regions aligned to the vessels highlighted in the **blue**, **red**, and **yellow boxed areas** shown at higher magnification (**L**, **M**, and **O**). OD, oculus dexter; OS, oculus sinister.

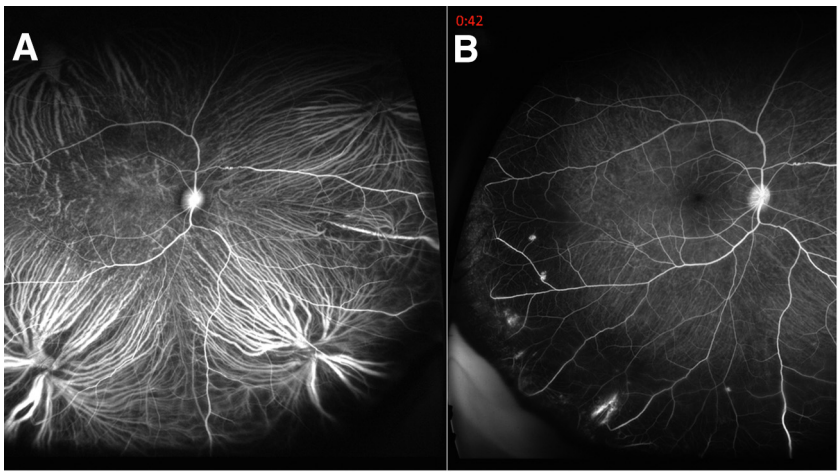

Figure 3 *In vivo* fluorescein angiograms observed in high-fat diet fed rhesus nonhuman primates (NHPs): fluorescein angiography imaging of two representative macaque monkeys 5 years after introduction to Western diet (WD). **A:** The initial choroidal flush after intravascular administration of fluorescein. **B:** Areas of breakdown of blood-retinal barrier as regions of hyperfluorescence in the peripheral retina. Because fluorescein binds to plasma albumin, sites of fluorescein leakage indicate sites of plasma leakage into retinal perivascular space. This feature mimics a similar sign seen in human diabetic retinopathy. No features of proliferative diabetic retinopathy are evident at this stage of the rhesus NHPs fed a WD.

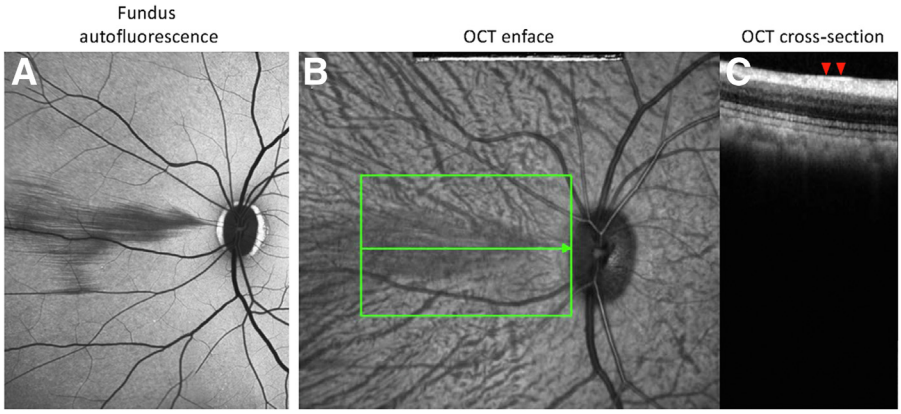

Figure 4 **A–C:** Fundus autofluorescence (**A**), optical coherence tomography (OCT) enface (**B**), and OCT cross-section (**C**) of a Western diet fed rhesus nonhuman primate 5 years after initiation of diet. **A** and **B:** Cotton-wool spots are clearly evident in the nasal region along the horizontal meridian adjacent to the optic disc. **B** and **C: Green boxed area** and **green horizontal line** (**B**) represent the level at which the OCT cross-section (**C**) was taken. OCT cross-section shows marked hyperreflectiveness (**red arrowheads**) in the nerve fiber layer.

In the middle and peripheral regions of the retina of T2D primates, the density of Iba-1$^+$ microglia/macrophage was significantly increased (Figure 9D) compared with controls (Figure 9C). Many of the Iba-1$^+$ microglia/macrophages changed their morphology from ramified to amoeboid, and the cells lost the regular distribution in stratum and spacing (Figure 9D) that is typical of ramified microglia (Figure 9C). Increased numbers of Iba-1$^+$ microglia/macrophages were typically seen in regions with fewer CD31$^+$ blood vessels (Figure 9D, compared with Figure 9C). Some of the Iba-1$^+$ microglia/macrophages demonstrated activated morphology with shorter processes and enlarged soma (Figure 9, B and D). The density of the Iba-1$^+$ cells was greater in the WD retinas compared with that in controls (Figure 9G). Many of the Iba-1$^+$ macrophages were detected in the ciliary bodies (Figure 9E) of the control NHPs. Although the number of Iba-1$^+$ macrophages in the ciliary body of the T2D mice was not statistically significant between the WD-fed and control animals, the intensity of the Iba-1$^+$ staining increased and the macrophages showed shorter and more prominent amoeboid processes (Figure 9, F and H).

GFAP$^+$ Astrocyte Intensity Is Increased in WD-Fed NHP Retinas Compared with Chow-Fed Controls

In the control retinas, GFAP$^+$ cells are only present in the ganglion cell and nerve fiber layers of the inner retinal region (Figure 10A). Consistent with earlier reports of astrocyte morphology in human, primate, and cat retinas,[23–26] GFAP$^+$ cells exhibit bipolar morphology with processes predominantly aligned to the axon bundles in the ganglion and nerve fiber layers of the central and middle (Figure 10C) retinal regions supportive of astrocytes. The GFAP$^+$ astrocytes gradually change to a stellate morphology in the periphery (Figure 10E). The highest concentration of GFAP$^+$

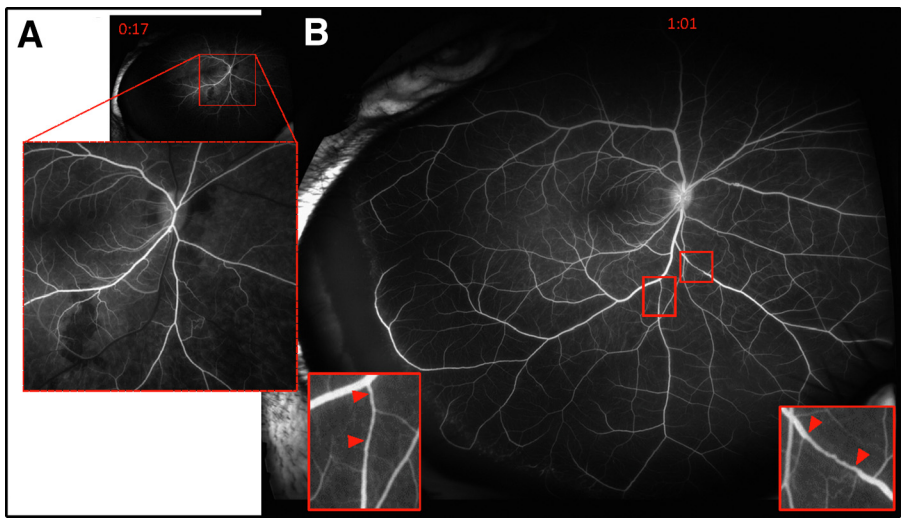

Figure 5 Representative fluorescein angiography of nonhuman primates that developed type 2 diabetes. Leaky vessels and hemorrhages are visible in the 17-second frame (**A**), whereas occluded vessels (**red arrowheads**) and venous tortuosity are evident distal to the occlusion (**insets**; **B**).

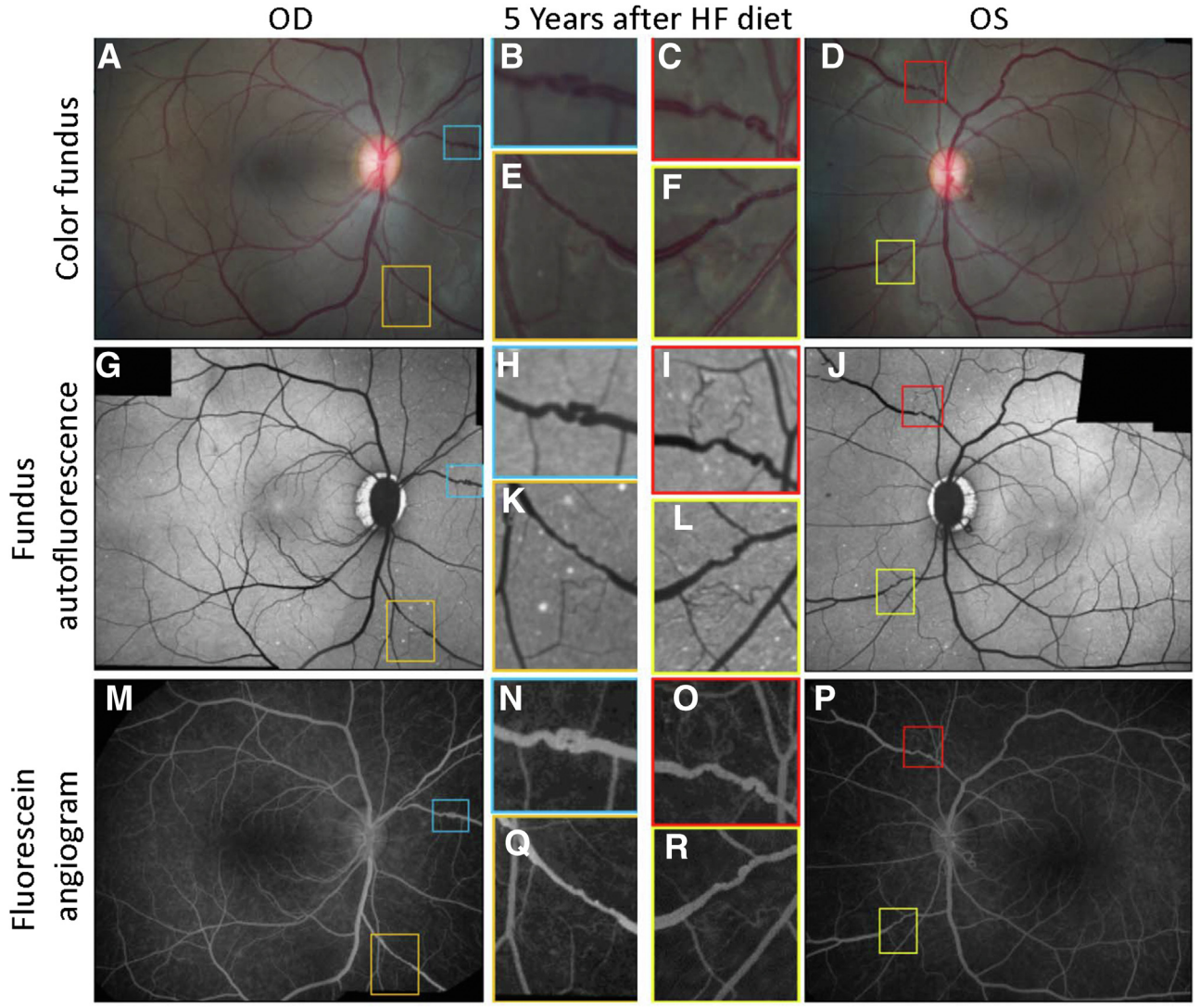

Figure 6 Representative color fundus (**A**–**F**), autofluorescence (**G**–**L**), and fluorescein angiography (**M**–**R**) images from nonhuman primates that developed type 2 diabetes. **Boxed areas** are magnified to demonstrate evidence of alterations in vessels, dot and blot hemorrhages (**G**, **K**, and **I**), and venous tortuosity (**B**, **C**, **E**, **F**, **H**, **I**, **L**, **N**, **O**, **Q**, and **R**). HF, high fat; OD, oculus dexter; OS, oculus sinister.

astrocytes is around the optic nerve head, and density decreases toward the periphery (compare Figure 10, C–E), as previously described.[23,24] In the WD-fed NHP retinas, astrocytes significantly increase their expression of GFAP in the region of the optic nerve, midretina, and peripheral retina (Figure 10, B, D, and F, comparing with Figure 10, A, C, E, and G).

Increased Vimentin Expression and Vessel Ensheathment by Müller Glia in WD-Fed NHP Retinas

In control retinas, lateral processes of vimentin$^+$ Müller cells demonstrated labeling primarily in the inner retina (Figure 11A). The present results confirmed previous reports showing a uniform topography of vimentin$^+$ Müller cells evenly distributed from central-mid (Figure 11C) to peripheral (Figure 11, E and G) regions.[27]

In WD-fed NHP retinas, Müller cell expression of vimentin is increased in cross-sections at the level of the inner nuclear layer (Figure 11B versus Figure 11A). The WD-fed samples showed enhanced vimentin$^+$ Müller cell processes ensheathing intraretinal vessels of larger caliber (Figure 11, B, D, and F, comparing with Figure 11, A, C, E, and G) in retinal whole-mount images. Ensheathment by vimentin$^+$ Müller cell processes along vessel segments was observed in the peripheral retina of WD-fed NHPs (Figure 11, F and H, comparing with Figure 11, E and G).

Marked Decrease in NeuN$^+$ Cells in Ganglion Cell Layer and Loss of Structural Integrity of Rod Outer Segments of WD-Fed NHP Retina

In control retinas, many NeuN$^+$ neurons are regularly distributed in the ganglion cell layer (Figure 12A). In

Table 1 Characteristics of Nonhuman Primates

Characteristic	WD (n = 7)	Chow (n = 6)	Reference controls (n = 20)
BW at time of T2D diagnosis, kg	18.8 ± 2.6	N/A	N/A
BW at time of necropsy, kg	14.7 ± 2.7	6.3 ± 1.3	
Glucose (fasting), mg/dL	160.7 ± 65.6	71.5 ± 27.5	54.4 ± 5.78
HOMA-IR	74.0 ± 77.1		2.78 ± 1.95
HbA1c at time of T2D diagnosis, %	11.4 ± 2.2		5.0 ± 0.6
Body fat at time of T2D diagnosis, %	41.7 ± 2.3		20.2 ± 6.6
Cholesterol at time of T2D diagnosis, mg/dL	189 ± 38	113 ± 37	
Triglyceride at time of T2D diagnosis, mg/dL	225 ± 151	51.8 ± 24.8	

Data are given as means ± SD.

BW, body weight; HbA1c, hemoglobin A1c; HOMA-IR, homeostatic model assessment for insulin resistance; N/A, not applicable; T2D, type 2 diabetes; WD, Western diet.

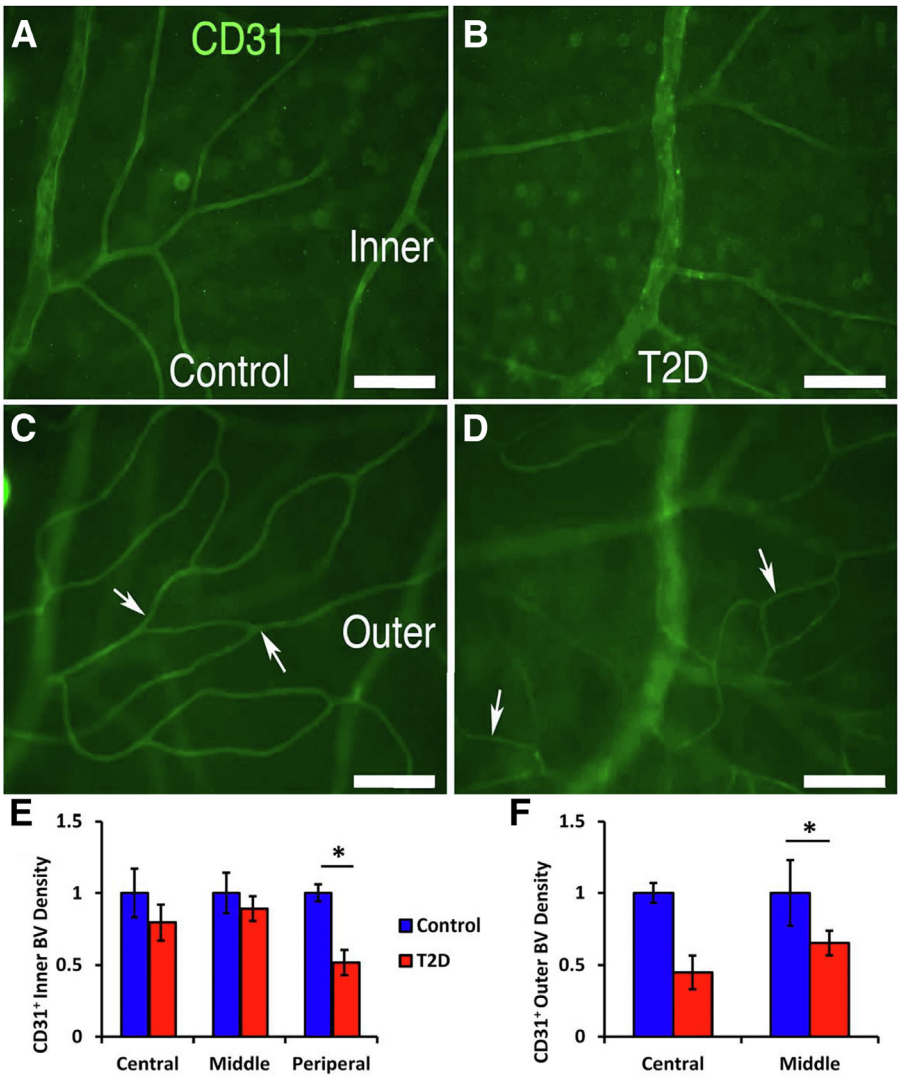

Figure 7 $CD31^+$ blood vessel (BV) density is decreased in type 2 diabetes (T2D) retina. The density of $CD31^+$ blood vessels decreased and $CD31^+$ capillaries in the outer plexus became thinner and less bright in T2D retina compared with control. **A**–**D:** Retinal flat mounts from the midperiphery of rhesus T2D nonhuman primates and control retinas: control (**A** and **C**) and T2D (**B** and **D**) stained with CD31 (green). **A** and **C** or **B** and **D:** Taken from the same region. **A** and **B:** Focus on inner blood vessel plexus. **C** and **D:** Focus on outer blood vessel plexus. **C** and **D: Arrows** indicate the $CD31^+$ outer plexus capillaries. **E:** The quantitative data of inner blood vessel density. **F:** The quantitative data of outer blood vessel density. *$P < 0.05$. Scale bars = 100 μm (**A**–**D**).

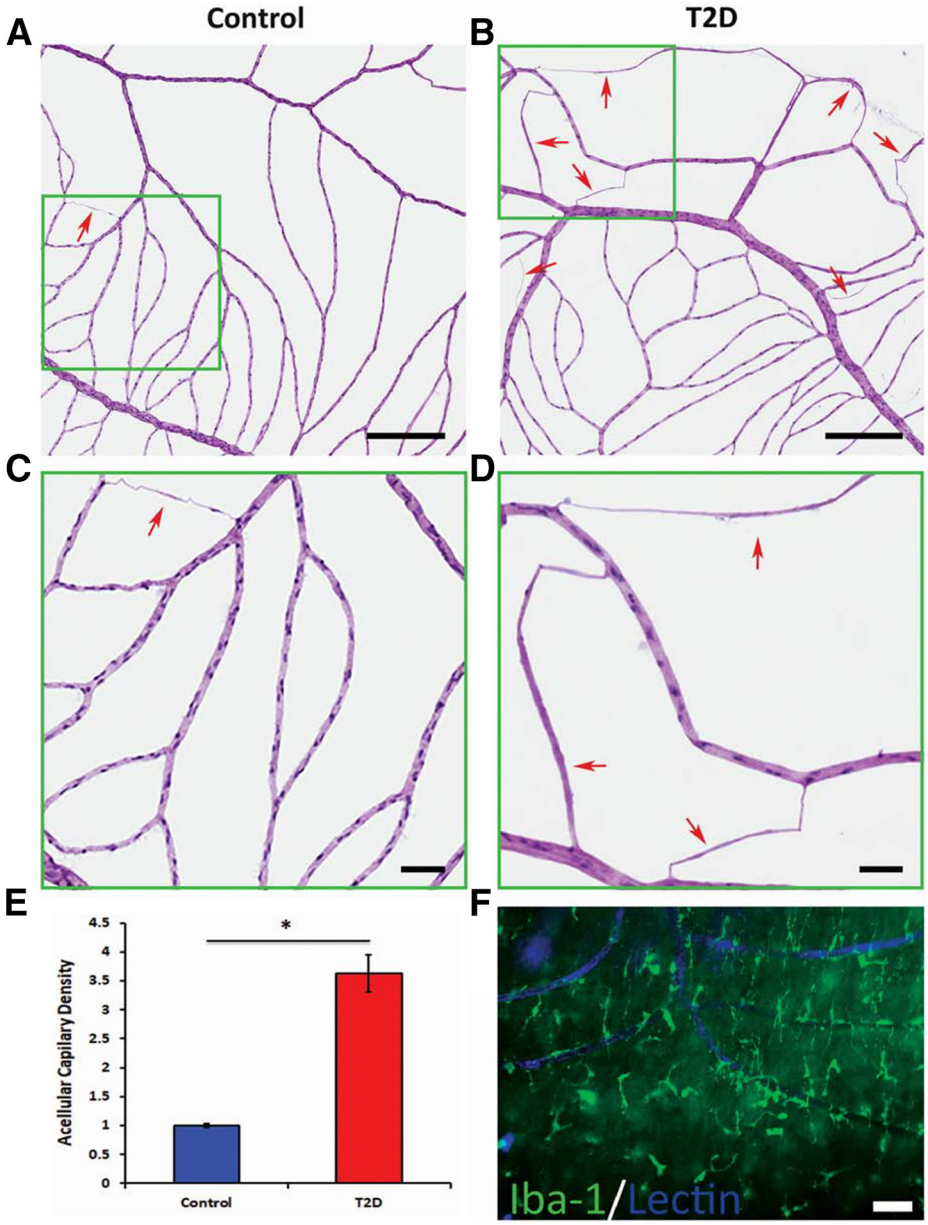

Figure 8 The number of acellular capillaries is increased in type 2 diabetes (T2D) retina. **A**–**D:** Trypsin-digested retinas were stained with hematoxylin and eosin. **A**–**D:** Compared with control (**A** and **C**) retinas, the T2D primate retinas (**B** and **D**) showed an increased number of acellular capillaries. **C** and **D:** High-magnification images from selective areas (**green boxed areas**) from **A** and **B**, respectively. **A**–**D: Arrows** indicate acellular capillary. **E:** The quantitative data. **F:** Retinal flat mounts from peripheral region of T2D nonhuman primate retina stained with ionized calcium-binding adaptor molecule 1 (Iba-1; green) and biotinylated *Griffonia simplicifolia* (*Bandeiraea*) isolectin B4 (lectin; blue), demonstrating copious numbers of Iba-1$^+$ microglia surrounding lectin$^+$ blood vessels. *$P < 0.05$. Scale bars: 500 μm (**A** and **B**); 100 μm (**C** and **D**); 50 μm (**F**).

contrast, the T2D retinas showed about a 50% reduction in the density of NeuN$^+$ neurons (Figure 12).

Rho is an opsin protein that labels rod outer segments.[28] In control retinas, Rho immunoreactivity was evenly distributed in fiber-like structures (Figure 13, A and C). In the WD-fed retinas, Rho$^+$ staining became irregular and uneven (Figure 13, B and D, comparing with Figure 13, A and C) with a 31% reduction in staining intensity (Figure 13E), suggestive of a loss of structural integrity of rod outer segments.

Iba-1 Expression and Lipofuscin-Like Granules Increase in RPE Cells of WD-Fed Animals

In control NHP eyes, Iba-1 consistently labeled the microglia/macrophages, whereas the RPE cells were consistently negative for this marker (Figure 14A). Autofluorescent granules were evident under all laser excitation wavelengths because of the autofluorescence from lipofuscin granules in RPE cells.[20] By way of example,

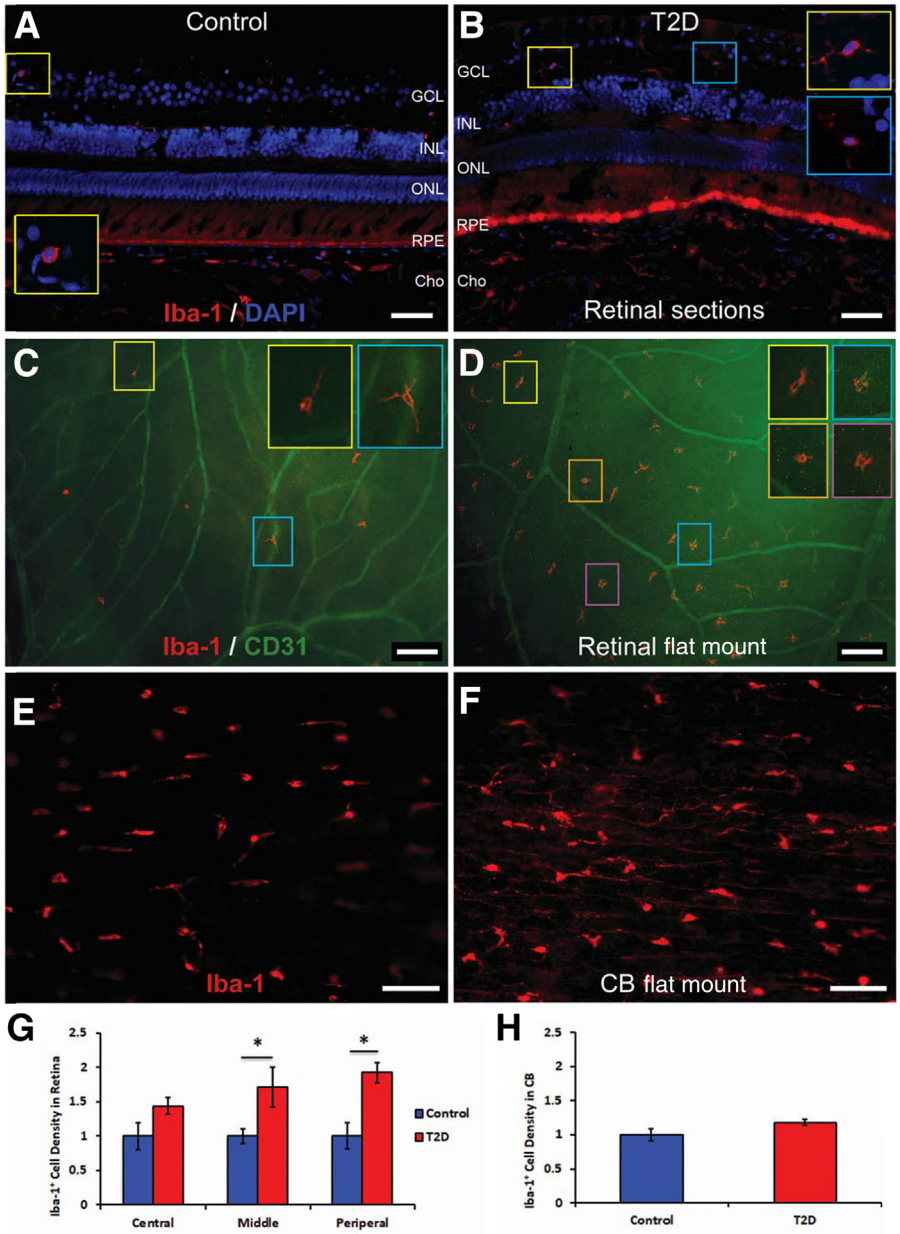

Figure 9 Ionized calcium-binding adaptor molecule 1—positive (Iba-1$^+$) microglia/macrophage density is increased in type 2 diabetes (T2D) retina compared with controls. **A** and **B:** Retinal sections from midperiphery regions of rhesus nonhuman primates (NHPs): control (**A**) and T2D (**B**) double stained with Iba-1 (red) and DAPI (blue). **C** and **D:** Retinal flat mount from middle-peripheral region of rhesus NHPs: control (**C**) and T2D (**D**) stained with Iba-1 (red) and CD31 (green). **E** and **F:** Ciliary body flat-mount control (**E**) and T2D (**F**) single stain using Iba-1 (red). **G:** The retinal quantitative data. **H:** The ciliary body quantitative data. **A**—**D** and **G:** Iba-1$^+$ microglia/macrophage density increases significantly in midperiphery and peripheral regions of the T2D retina. **E**, **F**, and **H:** Iba-1$^+$ macrophages increase their size and brightness with prominent processes in the ciliary body of T2D NHP nonhuman primates (**F**) comparing with controls (**E**); however, the Iba-1$^+$ macrophage density did not increase, leading us to suggest that Western diet induced activation of the resident microglia/macrophage population without recruitment of circulating monocytes (**H**). *$P < 0.05$. Scale bars: 50 μm (**A** and **B**); 100 μm (**C** and **D**); 50 μm (**E** and **F**). CB, ciliary body; Cho, choroid; GCL, ganglion cell layer; INL, inner nuclear layer; ONL, outer nuclear layer; RPE, retinal pigment epithelium.

Figure 14, C, E, and G, shows the autofluorescence in the red and green channel, even without primary or secondary antibodies.

In WD-fed animals, RPE cells exhibited Iba-1 immunoreactivity in two of the three retinas examined (Figure 14, B, F, and J; for low-magnification images, see Figure 14B compared with Figure 14A). Increased numbers of lipofuscin granules (Figure 14, D, F, and H) were associated with this Iba-1 immunoreactivity when compared with control (Figure 14I). This finding of increased lipofuscin accumulation in the WD-fed NHPs is similar to age-related changes in the human as lipofuscin represents the by-product of incomplete digestion of rod outer segments.[19]

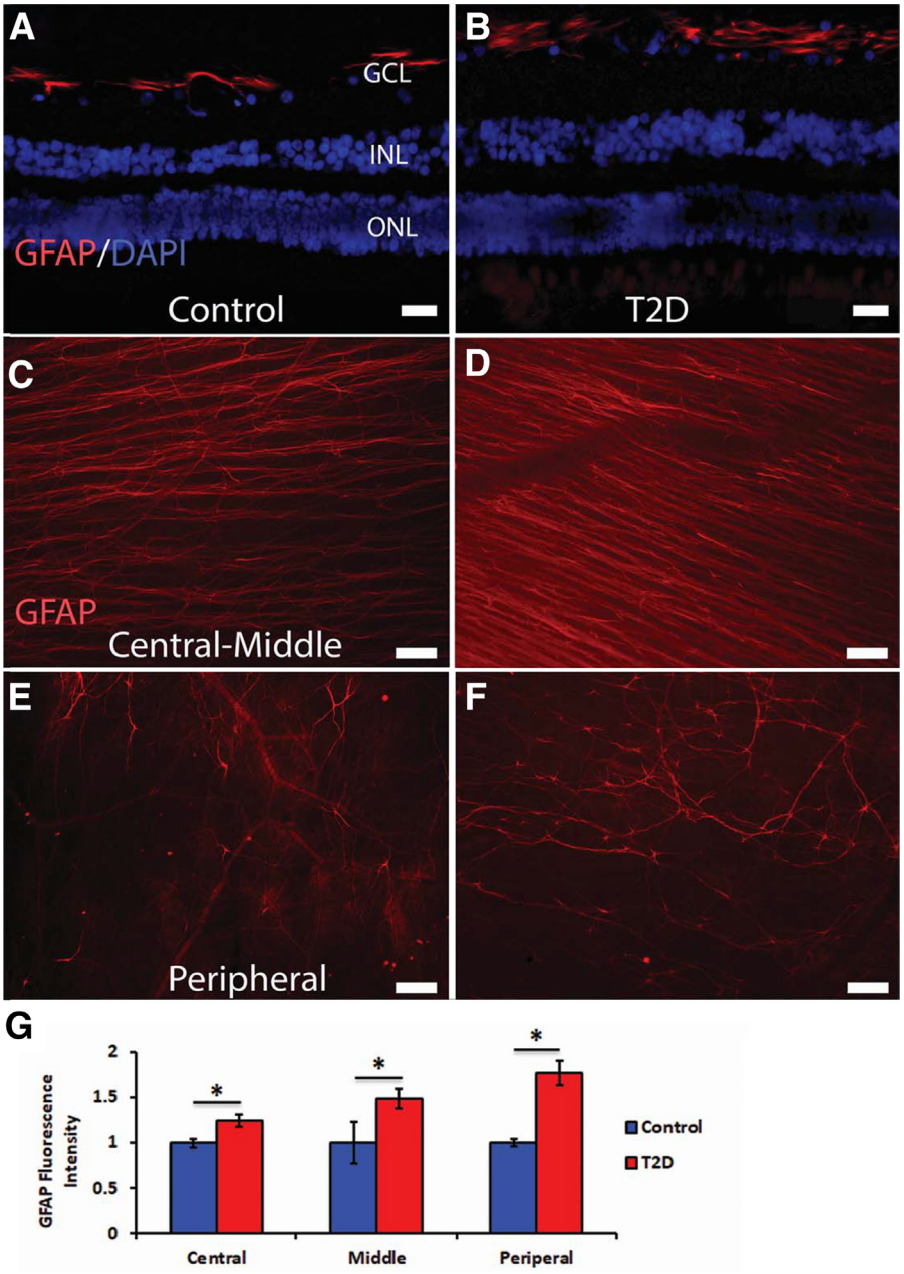

Figure 10 Glial fibrillary acidic protein—positive (GFAP$^+$) astrocyte intensity increases across type 2 diabetes (T2D) retina. **A** and **B:** Retinal cross-sections from middle region of control (**A**) and T2D (**B**) using GFAP (red) and DAPI (blue) staining. **C**—**F:** Retinal flat mounts from control (**C** and **E**) and T2D (**D** and **F**) stained with GFAP (red) are from central-middle region (**C** and **D**) and from peripheral region (**E** and **F**). **G:** The quantitative data confirming that GFAP$^+$ astrocyte intensity increased over the entire T2D retina compared with control. *$P < 0.05$. Scale bars: 20 μm (**A** and **B**); 100 μm (**C**—**F**). GCL, ganglion cell layer; INL, inner nuclear layer; ONL, outer nuclear layer.

Increased AQP4 Expression on Retinal Astrocytes and Müller Glia in T2D

AQP4 belongs to the aquaporin family of integral membrane proteins that form pores/channels in the membrane of biological cells, facilitating transport of water between cells. AQP4 is highly expressed on the abluminal processes of astrocytes abutting cerebral microvasculature. In control retinas, AQP4$^+$ expression was seen mainly in the inner retina, especially in the nerve fiber layer and surrounding blood vessels (Figure 15A). AQP4$^+$ expression was evident throughout the retina, with stronger expression in the central-mid region (Figure 15, C and E) and lower AQP4$^+$ expression in the periphery (data not shown). Consistent with earlier reports,[29,30] AQP4$^+$ expression was evident on both GFAP$^+$ astrocytes (Figure 15C) and vimentin$^+$ Müller cells (Figure 15E).

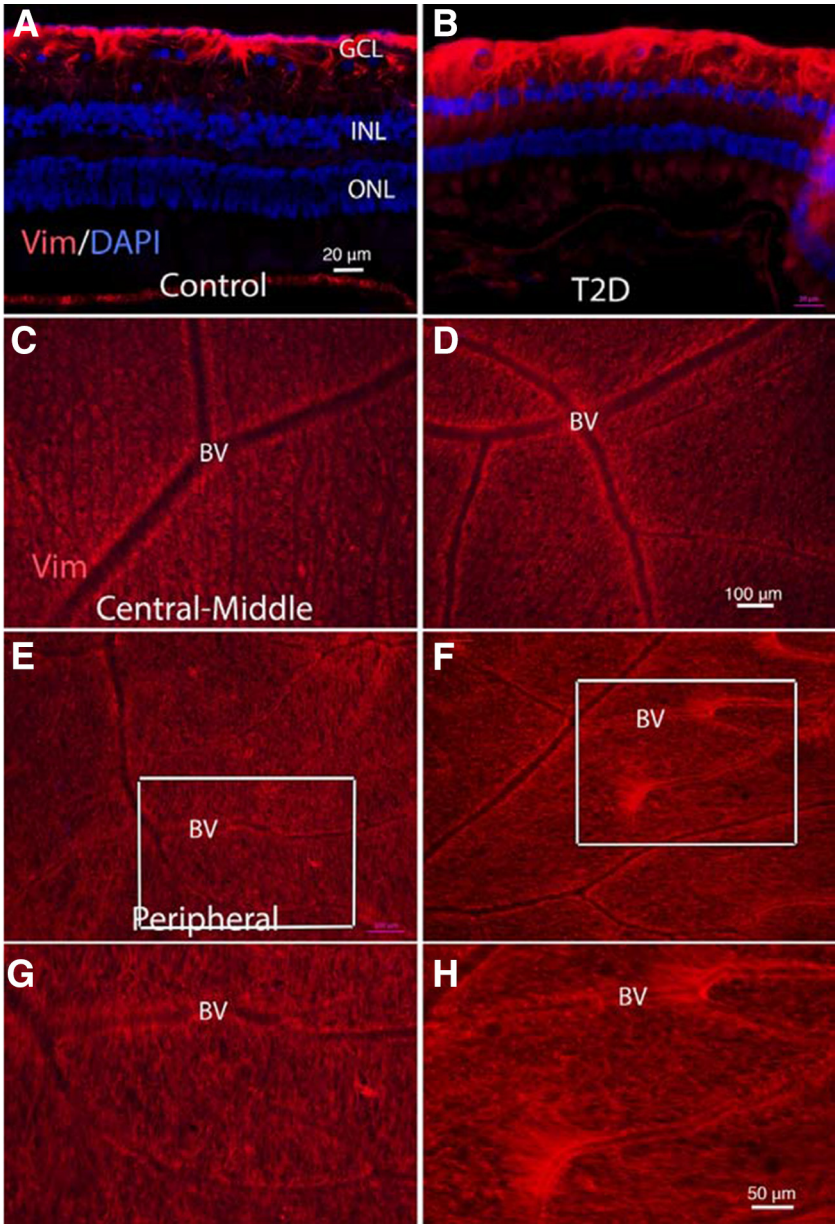

Figure 11 Vimentin (Vim)$^{+}$ Müller cells surrounding blood vessels (BVs) in type 2 diabetes (T2D) retina. **A** and **B:** Retinal sections from the mid region of control (**A**) and T2D (**B**) were stained with vimentin (red) and DAPI (blue). **C**—**H:** Retinal flat mounts of control (**C**, **E**, and **G**) and T2D (**D**, **F**, and **H**), demonstrating staining with vimentin (red). **C** and **D:** Sections are from central-mid region. **E** and **F:** Sections are from peripheral region. **G:** Represents the **boxed area** from **E**. **H:** Represents the **boxed area** from **F**. Vimentin^{+} Müller cells are distributed along the blood vessels in the T2D nonhuman primate retina. Scale bars: 20 μm (**A**, for **A** and **B**); 100 μm (**D**, for **C**—**F**); 50 μm (**H**, for **G** and **H**). GCL, ganglion cell layer; INL, inner nuclear layer; ONL, outer nuclear layer.

In the WD-fed retinas, the bright AQP4^{+} expression was more intense and expansive from the nerve fiber layer to the inner nuclear layer (Figure 15B compared with Figure 15A). AQP4^{+} expression was observed on the processes of both GFAP^{+} astrocytes and vimentin^{+} Müller cells and was more prominent than in the control retinas (Figure 15, D and F, compared with Figure 15, C and E). AQP4^{+} intensity in the central and peripheral regions (Figure 15G) and along the large blood vessels in central-middle regions (Figure 15H) of WD-fed retina was significantly greater than in controls.

Discussion

In the NHPs, T2D was induced by WD feeding for >5 years. The diet was like human high-fat diets that induce T2D.[31] All the NHPs on a WD became obese, hyperglycemic, hypertriglyceridemic, and hypertensive, and developed T2D (eg, fasting glucose >7 mmol or >126 mg/dL). Meanwhile, the controls had normal glucose, lipids, and blood pressure. Many salient features of human DR were observed in the WD-fed NHPs, including venous engorgement and tortuosity, exudates, and vascular leakage; nerve

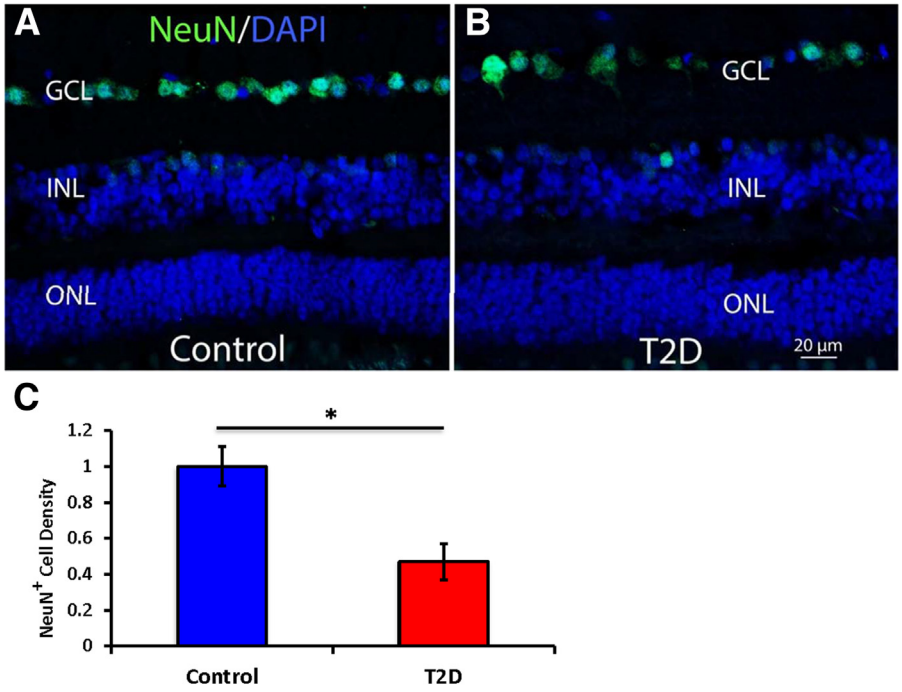

Figure 12 Neuronal nuclei antibody—positive (NeuN$^+$) neuronal density is decreased in type 2 diabetes (T2D) retina. Retinal cross-section from the mid region of nonhuman primate retina: control (**A**) and T2D (**B**) double stained with NeuN (green) and DAPI (blue). NeuN$^+$ neurons are uniformly located in ganglion cell layer (GCL) in control (**A**), but their density is decreased in T2D (**B**) retina comparing with control (**C**). *$P < 0.05$. Scale bar = 20 μm (**B**, for **A** and **B**). INL, inner nuclear layer; ONL, outer nuclear layer.

fiber infarction was observed less frequently. The NHPs showed vascular changes in the superficial retinal vessels, consisting of decreased blood vessel density in the peripheral retina. The deep vascular layer demonstrated reduced vascular density in the central retina. Consistent with other NHP DR models, the diabetic NHPs showed an increase in acellular capillaries. WD-induced diabetic NHPs demonstrated increased Iba-1$^+$ cell density, RPE with increased lipofuscin-like granules, and increased GFAP, vimentin, and AQP4 intensity compared with controls. Prolonged WD feeding resulted in neuronal loss in the ganglion cell layer and in the ONL compared with standard chow-fed NHPs. These findings support the marked similarity observed in the retinas of humans with T2D and the WD-fed NHPs studied here.

The significance of this study lies in the extensive use of multimarker immunofluorescence on both retinal whole mounts and frozen sections for colocalization of multiple cell types from distinct lineages in the retina, RPE, and ciliary body. This helped compare changes in multiple cell types within each part of the eye.

Vascular damage in obesity and diabetes results from increased cellular oxidative stress, activation of protein kinase C, release of superoxide, and production of advanced glycation end products, advanced lipoxidation end products, oxidized low-density lipoproteins and their receptors, and reactive oxygen species.[5,32–35] These mediators, when in excess, can induce microvascular dysfunction, activate glial cells, and promote neuronal loss in the diabetic retina.[34–36] Activated microglia express high levels of IL-12, IL-23, tumor necrosis factor-α, IL-1β, and IL-6,[37] which damage pericytes and endothelial cells, causing vascular dysfunction.[38] In DR, macroglia, such as astrocytes, become activated and secrete proinflammatory mediators, including IL-6, CXCL-2, and vascular endothelial growth factor.[39,40]

Activation of microglia can directly influence Müller cells via bidirectional signaling between the two cell types. Müller cells can further increase the state of activation of microglia by increasing their migration and adhesive cell contacts.[41] Müller cells have been strongly implicated in the neurodegeneration associated with DR. In DR, Müller cells express reduced levels of glutamine synthetase that converts the potentially toxic glutamate into glutamine.[42–44] Activated microglia are also a source of glutamate, reactive oxygen species, increased caspase 3, matrix metalloproteinases, and nitrous oxide. All of these are considered neurotoxic mediators involved in neurodegeneration.[45] Neuronal damage, chronic neurodegeneration, and dying cells, in turn, further activate the microglia,[46] which is a major driver of DR.[6,47]

The marked increase in fundus autofluorescence observed in the T2D eyes in this study is likely due to lipofuscin accumulation in the RPE.[48] Lipofuscin, a by-product of incomplete digestion of ingested photoreceptor outer segments,[48] was increased in T2D NHP retinas. DR is associated with changes in the subcellular structure of RPE cells and alterations of their secretome, which fosters the breakdown of the outer blood-retinal barrier.[49,50] Accumulation of lipofuscin within the RPE is associated with RPE

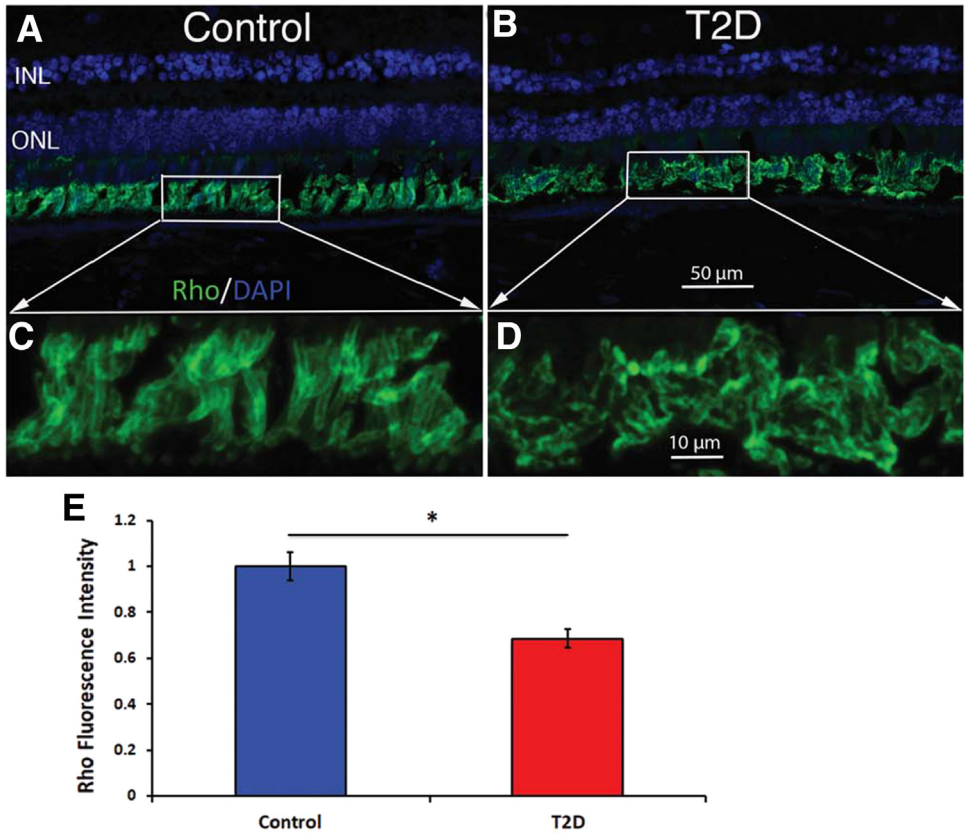

Figure 13 **A**–**D:** Rhodopsin (Rho)$^+$ immune staining in rod outer segments. Retinal sections from midperipheral regions of nonhuman primates (NHPs): control (**A** and **C**) and type 2 diabetes (T2D; **B** and **D**). **A** and **B:** Double stained with Rho (green) and DAPI (blue). **C** and **D:** Enlarged images of the **boxed areas** in **A** and **B**. Comparison of panels (**C** and **D**) shows a reduction in Rho$^+$ immune intensity as well as a loss of the vertical orientation of the rod outer segments in T2D NHPs compared with control. **E:** The quantitative plot demonstrating that Rho$^+$ immune-staining intensity was reduced by about 31% in T2D NHPs comparing with control and is statistically significant. *$P < 0.05$. Scale bars: 50 μm (**B**, for **A** and **B**); 10 μm (**D**, for **C** and **D**). INL, inner nuclear layer; ONL, outer nuclear layer.

dysfunction.[51] Lipofuscin accumulation, as observed in the current study, may serve to compromise the RPE cells' capacity to phagocytose rod outer segments, which, in turn, compromises RPE and photoreceptor function. Interestingly, the RPE cells in the diabetic NHPs became Iba-1 positive. Iba-1 is a cytoplasmic signaling protein that is primarily expressed in macrophages/microglia and is upregulated during their activation. However, Iba-1 can be expressed by other cells in response to injury[52] and is associated with cell proliferation and migration.[53] Together with reports from earlier work, the current findings indicate that a WD causes significant stress in RPE cells, resulting in their activation.

AQP4, a water channel protein, facilitates the movement of fluid across cell membranes.[54] AQP4 is highly expressed on the abluminal processes of astrocytes abutting cerebral microvasculature. AQP4 has been implicated in several pathophysiological processes. Recent evidence suggests AQP4 is involved in diverse functions, including neuroinflammation, cell migration, and Ca^{2+} signaling.[55] In the current study, AQP4$^+$ was increased in central and peripheral regions and along large blood vessels (Figure 15) of the diabetic NHPs. Polymorphisms exist in the *AQP4* gene that are associated with increased expression and the presence of diabetic retinopathy.[56] Vujosevic et al[57] showed that AQP4 levels increased 25-fold in the aqueous humor of diabetics with DR and sixfold in diabetics without DR compared with controls. Elevation in AQP4 has been associated with hypertension. However, in the study by Vujosevic et al,[57] no statistical difference in blood pressure was observed between controls and diabetics; but the use of antihypertensive medications was not recorded in this study. Animal models, including both spontaneous diabetic and streptozotocin (STZ)–induced diabetic rats, have been associated with increased retinal AQP4 expression,[58–62] which can be reduced by administration of the anti-inflammatory drug, minocycline.[58,59] However, other studies showed reduced AQP4 in db/db mice[63] and in STZ diabetic rats.[56] Results in rat Müller cell cultures suggest that activation of AQP4 was most affected by glucose variability and a different susceptibility, depending on the basal glucose conditions.[64]

Although DR in humans is clinically and histologically well characterized,[65] less is known about retinal findings in NHP experimental models of diabetes. Jonasson et al[66]

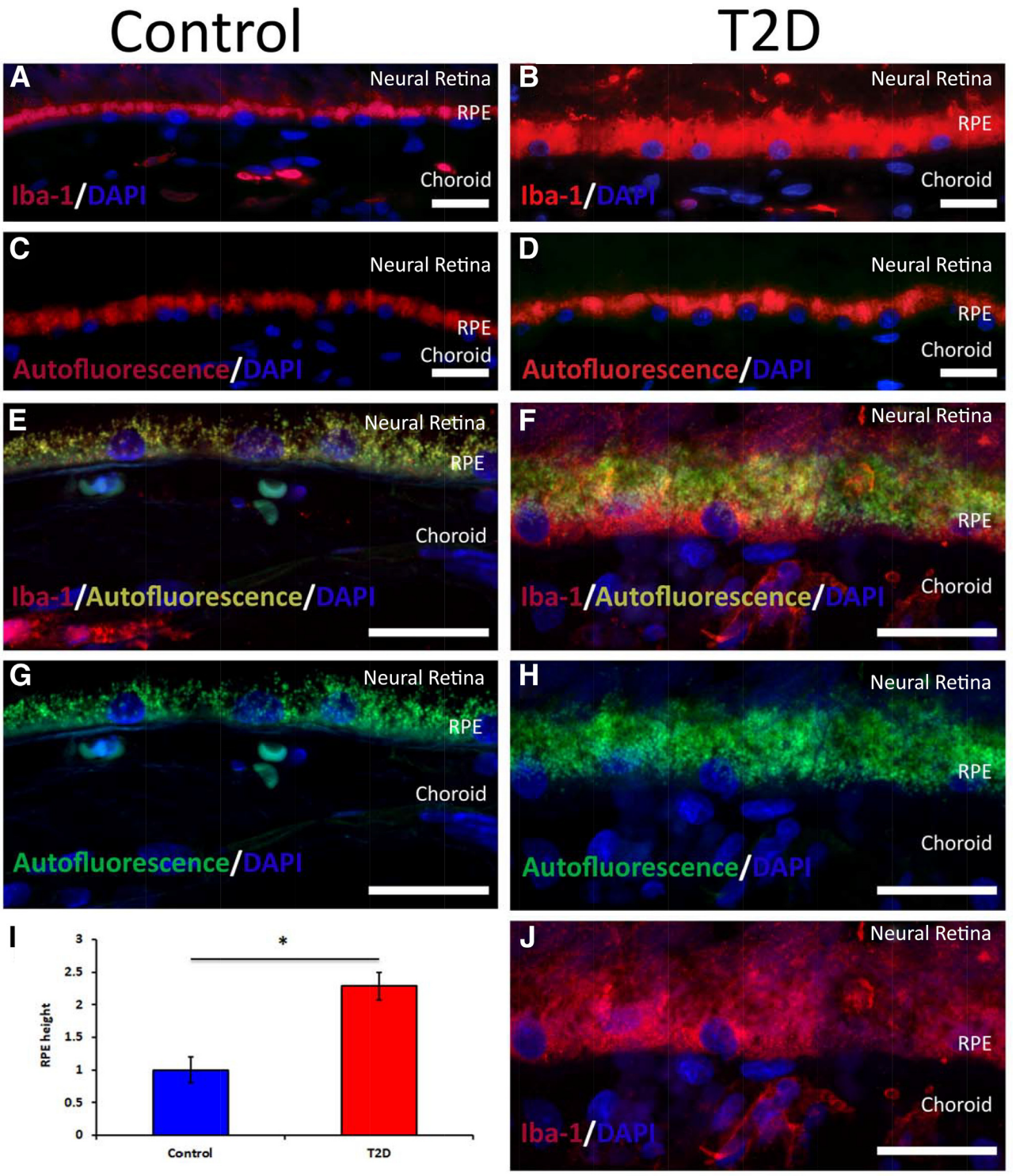

Figure 14 Retinal pigment epithelium (RPE) cells expressed ionized calcium-binding adaptor molecule 1 $(Iba\text{-}1)^{+}$ and increased numbers of lipofuscin-like granules in type 2 diabetes (T2D). Retinal sections from midperipheral region of rhesus nonhuman primates (NHPs). **A**, **C**, **E**, and **G:** Controls. **B**, **D**, **F**, **H**, and **J:** T2D. **A** and **B:** Stained with Iba-1 (red) and DAPI (blue). **C** and **D:** Represent adjacent sections of **A** and **B** and were stained only with DAPI (blue). Images show autofluorescent granules (red channel). **E** and **F:** Stained with Iba-1 (red) and DAPI (blue). Images show autofluorescent granules (green channel). **G** and **H:** Same images as **E** and **F**, but only with the green filter and DAPI. **I:** Increase in the relative thickness of the lipofuscin layer in the Western diet—fed animals compared with chow-fed controls. **J:** Same image as **F** but only showing Iba-1 and DAPI. Data are shown using adjacent sections and the same images with different combinations of filters intended to show the autofluorescence granules and Iba-1^{+} labeling more clearly. Images suggest that RPE cells become Iba-1^{+} and contain more lipofuscin-like granules in the T2D nonhuman primate. To quantitate the change of lipofuscin-like granules, the thickness of lipofuscin-like granules in the RPE cells of control and T2D NHP were compared. **I:** The increased amount both in extent and density of lipofuscin-like granules in RPE of the T2D NHPs comparing with control. $*P < 0.05$. Scale bars = 20 μm (**A**—**H** and **J**).

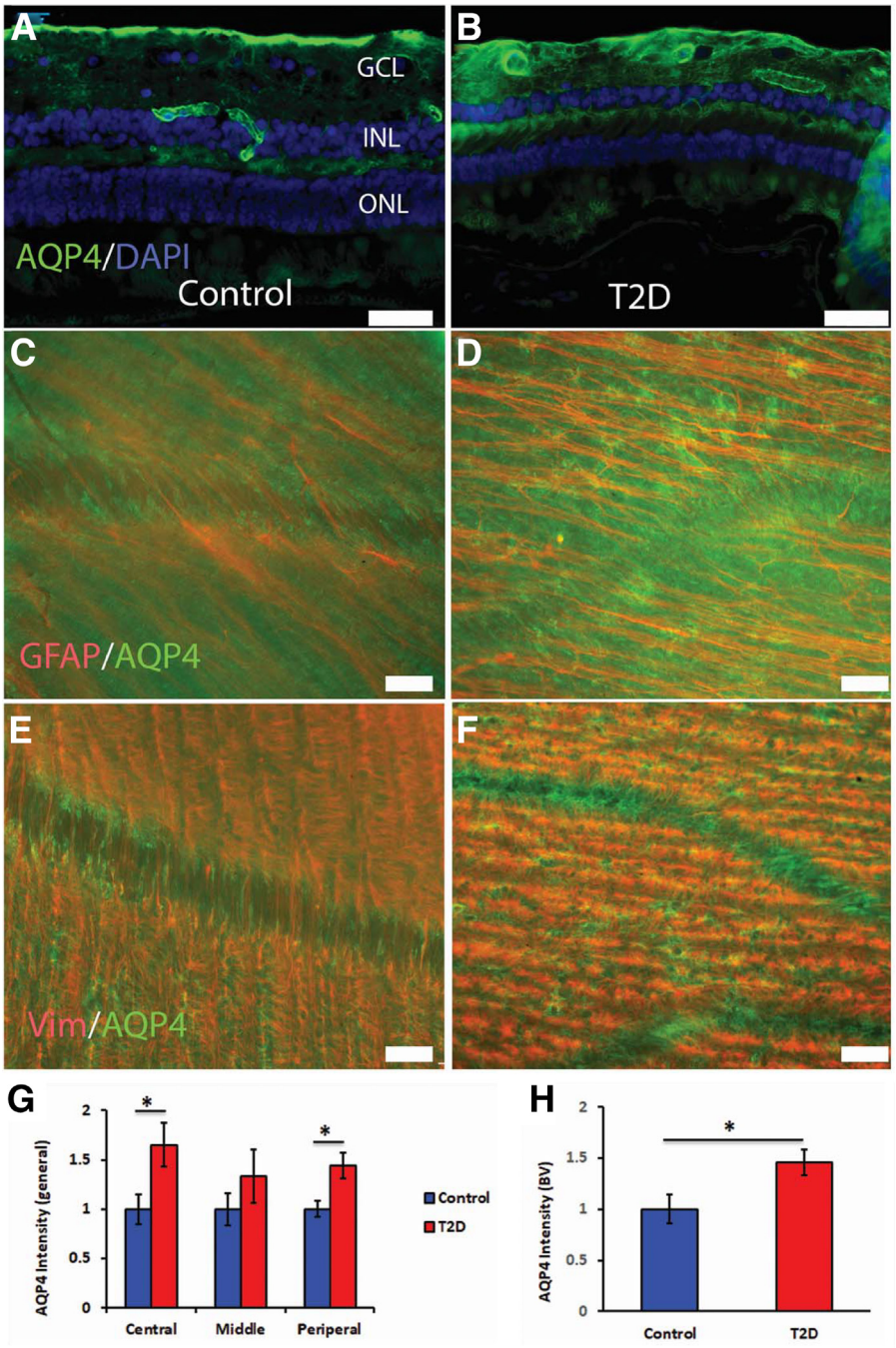

Figure 15 Aquaporin 4 (AQP4) expression on glial fibrillary acidic protein $(GFAP)^+$ astrocyte and vimentin $(Vim)^+$ Müller cells is increased in the type 2 diabetes (T2D) retina. **A** and **B:** Retinal cross-sections from the central-mid region of control (**A**) and T2D (**B**) nonhuman primate retinas triple stained with vimentin (red), AQP4 (green), and DAPI (blue). **C**—**F:** Retinal flat mounts of control (**C** and **E**) and T2D (**D** and **F**) retinas from the central-mid region. **C** and **D:** Double stained with GFAP (red) and AQP4 (green). **E** and **F:** Double stained with Vim (red) and AQP4 (green). **G:** The relative intensity of AQP4 expression in the different retinal regions. **H:** The relative intensity of AQP4 expression along blood vessel (BV). Images support that AQP4 expression is mainly in the inner portion of the retina and around BV and that AQP4 expression is on both $GFAP^+$ astrocytes and $vimentin^+$ Müller cells. In T2D retina, the AQP4 expression increased. **G** and **H:** Increased intensity of AQP4 expression in the central and peripheral regions of the retina and along the BV in T2D compared with controls. $^*P < 0.05$. Scale bars: 40 μm (**A** and **B**); 50 μm (**C**—**F**). GCL, ganglion cell layer; INL, inner nuclear layer; ONL, outer nuclear layer.

describe an 11-year study of rhesus monkeys with diabetes induced by either STZ or pancreatectomy. The NHPs had a duration of diabetes of up to 12.5 years, an average hemoglobin A1c of 14.3%, and marked elevations in triglycerides with normal or moderately increased cholesterol and no hypertension. Non-proliferative diabetic retinopathy was seen in these NHPs, including cotton-wool spots, degeneration of macular RPE, vascular leakage, attenuation of

vessels, and elevated posterior vitreous fluorescein levels correlating with blood-retinal barrier leakage.[67]

In the study by Tso et al,[13] the NHPs had various combinations of spontaneous diabetes or artificially induced diabetes utilizing STZ and fludrocortisone used for artificial induction of hypertension. Two groups of nonhypertensive monkeys with diabetes induced by either pancreatectomy or STZ induction showed no significant findings of DR by the end of the study. A two-monkey group with STZ-induced diabetes for an average of 13.5 and 15.9 years and spontaneous hypertension showed no signs of DR until the onset of hypertension. Once hypertensive, these NHPs showed signs of ischemic retinopathy, including peripapillary cotton-wool spots, atrophic maculae, capillary dropout on fluorescent angiography, focal capillary leakage, and reduced nasal ciliary artery hypoperfusion toward the end of their life. NHPs that spontaneously developed diabetes and then were given fludrocortisone to induce hypertension also demonstrated ischemic retinopathy with petechial hemorrhages, small focal intraretinal capillary leakage spots, cotton-wool spots, tortuosity and dilation of arterioles, exudates, and retinal atrophy, but only after induction of hypertension with fludrocortisone. Using a spontaneous model of diabetes and hypertension, Kim et al[10,11] demonstrated that the severely hypertensive and severely diabetic animals exhibited DR, whereas those with less severe hypertension and diabetes had less consistent retinal pathology. The findings of the above-mentioned studies demonstrate the importance of concomitant hypertension in initiating/driving the development of DR in NHPs.

Our study has some limitations, including the use of GFAP as a marker of both astrocytes and Müller cells. Although GFAP labels both astrocytes and activated Müller glia,[68–73] astrocytic labeling is distinguishable from Müller glia by virtue that astrocytic labeling is restricted to the nerve fiber layer and ganglion cell layer, where astrocytic processes are either stellate or closely ensheathed around the superficial retinal vascular plexus and nerve fiber bundles.[70] In contrast, Müller glial cells run radially throughout the entire thickness of the retina from the inner limiting membrane to the outer limiting membrane. Although both retinal macroglia share the ensheathment of the superficial plexus, ganglion cells, and nerve fiber bundles, the Müller glia have a uniform topography of distribution across the retina, whereas the astrocytes are centered more around the optic nerve head. Moreover, the two cell types have distinct process characteristics.[73] Thus, differences in morphology, topographic distribution, and residence in distinct strata of the retina allow use of GFAP to distinguish astrocytes from Müller cells.

In summary, this study in a WD-induced model of diabetes provides a unique description of retinal histologic changes, morphology, and localization not present in prior studies, while also reporting levels of hyperglycemia and hyperlipidemia, body fat percentages, and body weight, as well as duration of the diabetic state for these NHPs with DR. After the 5-year period of WD feeding, the NHPs experienced a similar degree of pathology that is seen in early to moderate non-proliferative diabetic retinopathy in humans, including venous engorgement and tortuosity, exudates, and vascular leakage; nerve fiber infarction was seen less frequently. On histologic assessment, the diabetic NHPs showed an increase in acellular capillaries, increased density of Iba-1$^+$ cell density, increased lipofuscin-like granules and changes in the subcellular structure of RPE, and disruption of the blood-retinal barrier[49,50] compared with controls. Moreover, the diabetic NHPs exhibited increased GFAP, vimentin, and AQP4 intensity compared with control animals. Finally, prolonged WD feeding resulted in neuronal loss in the ganglion cell layer and in the ONL. These findings support the marked similarity observed in the retinas of humans with T2D and the WD-fed NHPs studied here.

References

1. Donath MY, Shoelson SE: Type 2 diabetes as an inflammatory disease. Nat Rev Immunol 2011, 11:98–107
2. Nguyen DV, Shaw LC, Grant MB: Inflammation in the pathogenesis of microvascular complications in diabetes. Front Endocrinol (Lausanne) 2012, 3:170
3. Hammer SS, Beli E, Kady N, Wang Q, Wood K, Lydic TA, Malek G, Saban DR, Wang XX, Hazra S, Levi M, Busik JV, Grant MB: The mechanism of diabetic retinopathy pathogenesis unifying key lipid regulators, sirtuin 1 and liver X receptor. EBioMedicine 2017, 22: 181–190
4. Gregor MF, Hotamisligil GS: Inflammatory mechanisms in obesity. Annu Rev Immunol 2011, 29:415–445
5. Rains JL, Jain SK: Oxidative stress, insulin signaling, and diabetes. Free Radic Biol Med 2011, 50:567–575
6. Altmann C, Schmidt MHH: The role of microglia in diabetic retinopathy: inflammation, microvasculature defects and neurodegeneration. Int J Mol Sci 2018, 19:110
7. Chan-Ling T, McLeod DS, Hughes S, Baxter L, Chu Y, Hasegawa T, Lutty GA: Astrocyte-endothelial cell relationships during human retinal vascular development. Invest Ophthalmol Vis Sci 2004, 45: 2020–2032
8. Buchi ER, Kurosawa A, Tso MO: Retinopathy in diabetic hypertensive monkeys: a pathologic study. Graefes Arch Clin Exp Ophthalmol 1996, 234:388–398
9. Johnson MA, Lutty GA, McLeod DS, Otsuji T, Flower RW, Sandagar G, Alexander T, Steidl SM, Hansen BC: Ocular structure and function in an aged monkey with spontaneous diabetes mellitus. Exp Eye Res 2005, 80:37–42
10. Kim SY, Johnson MA, McLeod DS, Alexander T, Otsuji T, Steidl SM, Hansen BC, Lutty GA: Retinopathy in monkeys with spontaneous type 2 diabetes. Invest Ophthalmol Vis Sci 2004, 45: 4543–4553
11. Kim SY, Johnson MA, McLeod DS, Alexander T, Hansen BC, Lutty GA: Neutrophils are associated with capillary closure in spontaneously diabetic monkey retinas. Diabetes 2005, 54: 1534–1542
12. Robinson R, Barathi VA, Chaurasia SS, Wong TY, Kern TS: Update on animal models of diabetic retinopathy: from molecular approaches to mice and higher mammals. Dis Models Mechanisms 2012, 5: 444–456
13. Tso MO, Kurosawa A, Benhamou E, Bauman A, Jeffrey J, Jonasson O: Microangiopathic retinopathy in experimental diabetic monkeys. Trans Am Ophthalmol Soc 1988, 86:389–421
14. Kievit P, Halem H, Marks DL, Dong JZ, Glavas MM, Sinnayah P, Pranger L, Cowley MA, Grove KL, Culler MD: Chronic treatment

with a melanocortin-4 receptor agonist causes weight loss, reduces insulin resistance, and improves cardiovascular function in diet-induced obese rhesus macaques. Diabetes 2013, 62:490–497
15. Chan-Ling T: Glial, vascular, and neuronal cytogenesis in whole-mounted cat retina. Microsc Res Tech 1997, 36:1–16
16. Chan-Ling T, Page MP, Gardiner T, Baxter L, Rosinova E, Hughes S: Desmin ensheathment ratio as an indicator of vessel stability: evidence in normal development and in retinopathy of prematurity. Am J Pathol 2004, 165:1301–1313
17. Chang KH, Chan-Ling T, McFarland EL, Afzal A, Pan H, Baxter LC, Shaw LC, Caballero S, Sengupta N, Li Calzi S, Sullivan SM, Grant MB: IGF binding protein-3 regulates hematopoietic stem cell and endothelial precursor cell function during vascular development. Proc Natl Acad Sci U S A 2007, 104:10595–10600
18. Kuwabara T, Cogan DG: Studies of retinal vascular patterns, I: normal architecture. Arch Ophthalmol 1960, 64:904–911
19. Strauss O: The retinal pigment epithelium in visual function. Physiol Rev 2005, 85:845–881
20. Delori FC: Autofluorescence method to measure macular pigment optical densities fluorometry and autofluorescence imaging. Arch Biochem Biophys 2004, 430:156–162
21. Hughes S, Yang H, Chan-Ling T: Vascularization of the human fetal retina: roles of vasculogenesis and angiogenesis. Invest Ophthalmol Vis Sci 2000, 41:1217–1228
22. Provis JM, Diaz CM, Penfold PL: Microglia in human retina: a heterogeneous population with distinct ontogenies. Perspect Dev Neurobiol 1996, 3:213–222
23. Distler C, Kopatz K, Telkes I: Developmental changes in astrocyte density in the macaque perifoveal region. Eur J Neurosci 2000, 12: 1331–1341
24. Provis JM, Sandercoe T, Hendrickson AE: Astrocytes and blood vessels define the foveal rim during primate retinal development. Invest Ophthalmol Vis Sci 2000, 41:2827–2836
25. Chan-Ling T, Tout S, Hollander H, Stone J: Vascular changes and their mechanisms in the feline model of retinopathy of prematurity. Invest Ophthalmol Vis Sci 1992, 33:2128–2147
26. Chan-Ling T, Stone J: Degeneration of astrocytes in feline retinopathy of prematurity causes failure of the blood-retinal barrier. Invest Ophthalmol Vis Sci 1992, 33:2148–2159
27. Dreher Z, Robinson SR, Distler C: Muller cells in vascular and avascular retinae: a survey of seven mammals. J Comp Neurol 1992, 323:59–80
28. Ozawa Y, Nakao K, Kurihara T, Shimazaki T, Shimmura S, Ishida S, Yoshimura A, Tsubota K, Okano H: Roles of STAT3/SOCS3 pathway in regulating the visual function and ubiquitin-proteasome-dependent degradation of rhodopsin during retinal inflammation. J Biol Chem 2008, 283:24561–24570
29. Hamann S, Zeuthen T, La Cour M, Nagelhus EA, Ottersen OP, Agre P, Nielsen S: Aquaporins in complex tissues: distribution of aquaporins 1-5 in human and rat eye. Am J Physiol 1998, 274:C1332–C1345
30. Nagelhus EA, Veruki ML, Torp R, Haug FM, Laake JH, Nielsen S, Agre P, Ottersen OP: Aquaporin-4 water channel protein in the rat retina and optic nerve: polarized expression in Muller cells and fibrous astrocytes. J Neurosci 1998, 18:2506–2519
31. Andersen B, Straarup EM, Heppner KM, Takahashi DL, Raffaele V, Dissen GA, Lewandowski K, Bodvarsdottir TB, Raun K, Grove KL, Kievit P: FGF21 decreases body weight without reducing food intake or bone mineral density in high-fat fed obese rhesus macaque monkeys. Int J Obes (Lond) 2018, 42:1151–1160
32. Stitt AW, Curtis TM: Diabetes-related adduct formation and retinopathy. J Ocul Biol Dis Infor 2011, 4:10–18
33. Du XL, Edelstein D, Rossetti L, Fantus IG, Goldberg H, Ziyadeh F, Wu J, Brownlee M: Hyperglycemia-induced mitochondrial superoxide overproduction activates the hexosamine pathway and induces plasminogen activator inhibitor-1 expression by increasing Sp1 glycosylation. Proc Natl Acad Sci U S A 2000, 97:12222–12226
34. Hu P, Hunt NH, Arfuso F, Shaw LC, Uddin MN, Zhu M, Devasahayam R, Adamson SJ, Benson VL, Chan-Ling T, Grant MB: Increased indoleamine 2,3-dioxygenase and quinolinic acid expression in microglia and Müller cells of diabetic human and rodent retina. Invest Ophthalmol Vis Sci 2017, 58:5043–5055
35. Zong H, Ward M, Stitt AW: AGEs, RAGE, and diabetic retinopathy. Curr Diab Rep 2011, 11:244–252
36. Milne R, Brownstein S: Advanced glycation end products and diabetic retinopathy. Amino Acids 2013, 44:1397–1407
37. Martinez FO, Helming L, Gordon S: Alternative activation of macrophages: an immunologic functional perspective. Annu Rev Immunol 2009, 27:451–483
38. Yang LP, Sun HL, Wu LM, Guo XJ, Dou HL, Tso MO, Zhao L, Li SM: Baicalein reduces inflammatory process in a rodent model of diabetic retinopathy. Invest Ophthalmol Vis Sci 2009, 50:2319–2327
39. Shin ES, Huang Q, Gurel Z, Sorenson CM, Sheibani N: High glucose alters retinal astrocytes phenotype through increased production of inflammatory cytokines and oxidative stress. PLoS One 2014, 9: e103148
40. Nagayach A, Patro N, Patro I: Astrocytic and microglial response in experimentally induced diabetic rat brain. Metab Brain Dis 2014, 29: 747–761
41. Wang M, Ma W, Zhao L, Fariss RN, Wong WT: Adaptive Muller cell responses to microglial activation mediate neuroprotection and coordinate inflammation in the retina. J Neuroinflammation 2011, 8:173
42. Mizutani M, Gerhardinger C, Lorenzi M: Muller cell changes in human diabetic retinopathy. Diabetes 1998, 47:445–449
43. Lieth E, LaNoue KF, Antonetti DA, Ratz M; The Penn State Retina Research Group: Diabetes reduces glutamate oxidation and glutamine synthesis in the retina. Exp Eye Res 2000, 70:723–730
44. Rungger-Brandle E, Dosso AA, Leuenberger PM: Glial reactivity, an early feature of diabetic retinopathy. Invest Ophthalmol Vis Sci 2000, 41:1971–1980
45. Krady JK, Basu A, Allen CM, Xu Y, LaNoue KF, Gardner TW, Levison SW: Minocycline reduces proinflammatory cytokine expression, microglial activation, and caspase-3 activation in a rodent model of diabetic retinopathy. Diabetes 2005, 54:1559–1565
46. Kettenmann H, Hanisch UK, Noda M, Verkhratsky A: Physiology of microglia. Physiol Rev 2011, 91:461–553
47. Rubsam A, Parikh S, Fort PE: Role of inflammation in diabetic retinopathy. Int J Mol Sci 2018, 19:942
48. Sparrow JR, Boulton M: RPE lipofuscin and its role in retinal pathobiology. Exp Eye Res 2005, 80:595–606
49. Xu HZ, Song Z, Fu S, Zhu M, Le YZ: RPE barrier breakdown in diabetic retinopathy: seeing is believing. J Ocul Biol Dis Infor 2011, 4:83–92
50. Ponnalagu M, Subramani M, Jayadev C, Shetty R, Das D: Retinal pigment epithelium-secretome: a diabetic retinopathy perspective. Cytokine 2017, 95:126–135
51. Schmitz-Valckenberg S, Bultmann S, Dreyhaupt J, Bindewald A, Holz FG, Rohrschneider K: Fundus autofluorescence and fundus perimetry in the junctional zone of geographic atrophy in patients with age-related macular degeneration. Invest Ophthalmol Vis Sci 2004, 45:4470–4476
52. Autieri MV, Carbone C, Mu A: Expression of allograft inflammatory factor-1 is a marker of activated human vascular smooth muscle cells and arterial injury. Arterioscler Thromb Vasc Biol 2000, 20: 1737–1744
53. Tian Y, Jain S, Kelemen SE, Autieri MV: AIF-1 expression regulates endothelial cell activation, signal transduction, and vasculogenesis. Am J Physiol Cell Physiol 2009, 296:C256–C266
54. Verkman AS, Ruiz-Ederra J, Levin MH: Functions of aquaporins in the eye. Prog Retinal Eye Res 2008, 27:420–433
55. Nagelhus EA, Ottersen OP: Physiological roles of aquaporin-4 in brain. Physiol Rev 2013, 93:1543–1562
56. Wang T, Zhang C, Xie H, Jiang M, Tian H, Lu L, Xu GT, Liu L, Zhang J: Anti-VEGF therapy prevents Muller intracellular edema by decreasing VEGF-A in diabetic retinopathy. Eye Vis (Lond) 2021, 8:13

57. Vujosevic S, Micera A, Bini S, Berton M, Esposito G, Midena E: Aqueous humor biomarkers of Muller cell activation in diabetic eyes. Invest Ophthalmol Vis Sci 2015, 56:3913–3918
58. Zhang Y, Xu G, Ling Q, Da C: Expression of aquaporin 4 and Kir4.1 in diabetic rat retina: treatment with minocycline. J Int Med Res 2011, 39:464–479
59. Cui B, Sun JH, Xiang FF, Liu L, Li WJ: Aquaporin 4 knockdown exacerbates streptozotocin-induced diabetic retinopathy through aggravating inflammatory response. Exp Eye Res 2012, 98:37–43
60. Fukuda M, Nakanishi Y, Fuse M, Yokoi N, Hamada Y, Fukagawa M, Negi A, Nakamura M: Altered expression of aquaporins 1 and 4 coincides with neurodegenerative events in retinas of spontaneously diabetic Torii rats. Exp Eye Res 2010, 90:17–25
61. Oosuka S, Kida T, Oku H, Horie T, Morishita S, Fukumoto M, Sato T, Ikeda T: Effects of an aquaporin 4 inhibitor, TGN-020, on murine diabetic retina. Int J Mol Sci 2020, 21:2324
62. Kida T, Oku H, Horie T, Fukumoto M, Okuda Y, Morishita S, Ikeda T: Implication of VEGF and aquaporin 4 mediating Muller cell swelling to diabetic retinal edema. Graefes Arch Clin Exp Ophthalmol 2017, 255:1149–1157
63. Hanaguri J, Nagai N, Yokota H, Kushiyama A, Watanabe M, Yamagami S, Nagaoka T: Fenofibrate nano-eyedrops ameliorate retinal blood flow dysregulation and neurovascular coupling in type 2 diabetic mice. Pharmaceutics 2022, 14:384
64. Picconi F, Parravano M, Sciarretta F, Fulci C, Nali M, Frontoni S, Varano M, Caccuri AM: Activation of retinal Muller cells in response to glucose variability. Endocrine 2019, 65:542–549
65. Kempen JH, O'Colmain BJ, Leske MC, Haffner SM, Klein R, Moss SE, Taylor HR, Hamman RF: Eye Diseases Prevalence Research Group: The prevalence of diabetic retinopathy among adults in the United States. Arch Ophthalmol 2004, 122:552–563
66. Jonasson O, Jones CW, Bauman A, John E, Manaligod J, Tso MO: The pathophysiology of experimental insulin-deficient diabetes in the monkey: implications for pancreatic transplantation. Ann Surg 1985, 201:27–39
67. Zeimer RC, Cunha-Vaz JG, Johnson ME: Studies on the technique of vitreous fluorophotometry. Invest Ophthalmol Vis Sci 1982, 22: 668–674
68. Ling TL, Stone J: The development of astrocytes in the cat retina: evidence of migration from the optic nerve. Brain Res Dev Brain Res 1988, 44:73–85
69. Ling TL, Mitrofanis J, Stone J: Origin of retinal astrocytes in the rat: evidence of migration from the optic nerve. J Comp Neurol 1989, 286:345–352
70. Chan-Ling T, Stone J: Factors determining the migration of astrocytes into the developing retina: migration does not depend on intact axons or patent vessels. J Comp Neurol 1991, 303:375–386
71. Hollander H, Makarov F, Dreher Z, van Driel D, Chan-Ling TL, Stone J: Structure of the macroglia of the retina: sharing and division of labour between astrocytes and Muller cells. J Comp Neurol 1991, 313:587–603
72. Tout S, Chan-Ling T, Hollander H, Stone J: The role of Muller cells in the formation of the blood-retinal barrier. Neuroscience 1993, 55:291–301
73. Chan-Ling T: Glial, neuronal and vascular interactions in the mammalian retina. Prog Retin Eye Res 1994, 13:357–389